Paleoceanography and Paleoclimatology

RESEARCH ARTICLE
10.1029/2019PA003781

Special Section:
The Miocene: The Future of the Past

Orbital Forcing of Late Miocene–Early Pleistocene Environmental Change in the Zhada Basin, SW Tibetan Plateau

C. M. Saadeh[1], J. E. Saylor[2], J. Nie[3], and T. M. Shanahan[4]

[1]Department of Earth and Atmospheric Sciences, University of Houston, Houston, TX, USA, [2]Department of Earth, Ocean and Atmospheric Sciences, University of British Columbia, Vancouver, British Columbia, Canada, [3]Key Lab of Western China's Environmental Systems, Lanzhou University, Lanzhou, China, [4]Department of Geological Sciences, The Jackson School of Geosciences, University of Texas at Austin, Austin, TX, USA

Key Points:
- Isotope, sedimentology, and grain size data record low- and high-frequency Miocene–Pleistocene environmental change on the Tibetan Plateau
- All data record low-frequency tectonic and climate changes, whereas O isotope data document high-frequency changes at Milankovitch periods
- Anticorrelation between the isotope record and Northern Hemisphere insolation suggests insolation exerts a primary control on monsoon strength

Supporting Information:
- Supporting Information S1

Correspondence to:
C. M. Saadeh,
cmsaadeh@uh.edu

Citation:
Saadeh, C. M., Saylor, J. E., Nie, J., & Shanahan, T. M. (2020). Orbital forcing of late Miocene–early Pleistocene environmental change in the Zhada Basin, SW Tibetan Plateau. *Paleoceanography and Paleoclimatology*, *35*, e2019PA003781. https://doi.org/10.1029/2019PA003781

Received 7 OCT 2019
Accepted 28 MAY 2020
Accepted article online 11 JUN 2020

Abstract Mechanisms controlling the long- and short-term variability of the Indian Summer Monsoon (ISM) and high-elevation environmental change have largely been examined using low-elevation or marine records with less emphasis on high-elevation non-marine records. We address this using a high-resolution, long-term record from upper Miocene–lower Pleistocene (~9.0–2.2 Ma) fluvio-lacustrine strata in the Zhada Basin, southwestern Tibetan Plateau. Long-term changes include the onset of lacustrine deposition, a decrease in mean grain size, and an increase in $\delta^{18}O_{carb}$ and $\delta^{13}C_{carb}$ values at ~6.0 Ma in response to basin closure following regional extension. This was followed by a return to palustrine/fluvial deposition, an increase in mean grain size, and a decrease in $\delta^{18}O_{carb}$ and $\delta^{13}C_{carb}$ values at ~3.5 Ma in response to tectonically driven long-term ISM weakening. Spectral analysis reveals that high-frequency variations in the $\delta^{18}O_{carb}$ record are dominated by 100 and ~20 kyr cycles from ~6.0–2.2 Ma. Wavelet and spectral analysis of the most densely sampled interval (4.23–3.55 Ma), tuned to the record of daily insolation (21 June at 35°N) confirms and highlights 100 and 20 kyr cycles. The tuned Pliocene $\delta^{18}O_{carb}$ record is coherent with the record of Northern Hemisphere insolation at precession periods but not at obliquity or eccentricity periods. Additionally, the tuned $\delta^{18}O_{carb}$ record is anticorrelated to the insolation record, indicating that stronger Northern Hemisphere insolation correlates with a stronger ISM. These results suggest that variations in daily insolation drove late Miocene–early Pleistocene high-frequency ISM variability and environmental changes in the high-elevation southwestern Tibetan Plateau.

Plain Language Summary The Indian Summer Monsoon is a planetary-scale climate system. It currently affects >1.8 billion people, and changes in the monsoon likely led to major changes in plant and animal populations ~7 million years ago. Whether the Himalayan mountains, Tibetan Plateau, or the Southern Hemisphere are the major players in controlling the strength of the monsoon remains unclear. We address this question using the first long-term, high-resolution isotopic and sedimentological record from the Zhada Basin on the Tibetan Plateau. Changes in oxygen isotopes in carbonate rocks track the increase or decrease in precipitation amount. The frequency of the changes in the isotopic record match the frequency of changes in Earth's orbit. Changes in the isotope record also show that when the Tibetan Plateau received more sunlight, which is determined by changes in Earth's orbit, the monsoon was more intense. These observations point to the conclusion that Earth's orbit changes the solar heating received by the plateau surface, which in turn plays a major role in the amount of precipitation on the Tibetan Plateau.

1. Introduction

The Asian Monsoon System (AMS), and its subsystems the East Asian Monsoon (EAM) and Indian Summer Monsoon (ISM), affects a third of the world's population and is a fundamental component of Earth's modern climate. However, there is disagreement on the timing of initiation or secular changes in strength of the AMS and its driving mechanisms, particularly prior to Northern Hemisphere Glaciation. In this contribution, we address three outstanding questions regarding the AMS. First, what drove low- and high-frequency ISM variation prior to the onset and strengthening of Northern Hemisphere Glaciation in the middle Pliocene (Clift & Plumb, 2008; Gupta & Thomas, 2003; Mudelsee & Raymo, 2005). The second question is whether

strengthening of the ISM was directly driven by changes in Northern Hemisphere insolation or was an indirect response to Southern Hemisphere warming (Caley et al., 2011; Clemens & Prell, 2003; Gebregiorgis et al., 2018). Finally, it remains poorly understood whether the ISM and EAM respond to the same insolation forcing or if these systems evolved asynchronously. To address these questions, we use a high-resolution, long-term, non-marine record from Miocene–Pleistocene fluvio-lacustrine strata from the southern Tibetan Plateau.

Models of long-term (low-frequency) ISM variations are inconsistent in their attribution to Tibetan Plateau or Himalaya uplift. For example, the onset of monsoon circulation was proposed to coincide with late Miocene–Pliocene uplift of the Tibetan Plateau (Kroon et al., 1991; Prell & Kutzbach, 1992; Quade et al., 1995). However, several lines of evidence, including eolian deposits exposed NE of the Tibetan Plateau, suggest the initiation of a monsoon system occurred prior to 8 Ma and possibly by 24 Ma (e.g., Clift et al., 2002; Dettman et al., 2001; Garzione et al., 2005; Guo et al., 2002). Further deepening the divide between Tibetan Plateau uplift and monsoon initiation, many paleoelevation studies now point to high elevations in the southern Tibetan Plateau throughout the Cenozoic (e.g., DeCelles et al., 2007; Ding et al., 2014; Hoke et al., 2014; Su et al., 2019). Moreover, general circulation models indicate that an elevated Himalayan range alone is sufficient to block dry Westerly circulation and allow penetration of moisture on to the Indian and Asian land masses, obviating the need for a similarly elevated hinterland to account for changes in monsoon circulation (Boos & Kuang, 2010). However, models also suggest that the ISM response to mountain building is complex; surface uplift of the southern Tibetan Plateau and Zagros Mountains appears to strengthen the ISM while uplift of the central and northern Tibetan Plateau and the Tianshan Altai mountains weakens it (An et al., 2001; Tang et al., 2013; Zhang et al., 2015). The discrepancies in these studies call for greater resolution of climate change on the Tibetan Plateau and on the link between climate change and orogenic uplift.

In addition to the secular (i.e., low-frequency) changes noted above, multiple studies suggest that high-frequency (orbital or sub-orbital) variations in the strength of the AMS are correlated with changes in North Atlantic climate, orbitally driven changes in insolation, and sea surface temperatures (SSTs) in the Indian Ocean and Arabian Sea. For example, Feng and Hu (2008) argue that the Atlantic Multidecadal Oscillation (AMO) affects the strength of the ISM (quantified in their study as All India Monsoon Rainfall) by changing temperature on the Tibetan Plateau. Warm AMO phases correlate with a warmer Tibetan Plateau and therefore a stronger ISM due to the greater meridional temperature gradient between the Tibetan Plateau and the tropical Indian Ocean (Feng & Hu, 2008). Alternatively, recognizing that variation in the amount of solar insolation due to the configuration of Earth's orbit plays a role in the evolution of climate systems (Hays et al., 1976; Huybers, 2006; Milankovitch, 1941), Zhu et al. (2009) argue that high insolation directly enhances the ISM by radiative heating of the plateau, leading to wetter conditions on the Tibetan Plateau. In contrast, during periods with low insolation, the Westerlies strengthen and shift southward and modulate the impact of north Atlantic climate conditions on the Tibetan Plateau (Zhu et al., 2009). Westerly airmasses are significantly drier than ISM airmasses, and their dominance over the western Tibetan Plateau accounts for the observed westward increase in aridity on the Tibetan Plateau (Bookhagen & Burbank, 2010; Li & Garzione, 2017). In the late Holocene, decreasing lake levels on the Tibetan Plateau have been attributed to decreasing summer insolation and weakening of the ISM (Hudson & Quade, 2013; Morrill et al., 2006). Finally, the ISM also responds to changes in tropical Indian Ocean temperatures, with cooler temperatures correlating with weaker ISM and stronger EAM (Conroy & Overpeck, 2011; Wang et al., 2005). Mohtadi et al. (2014) provide a mechanism for this observation wherein southward penetration of the Westerlies and attendant southward displacement of the Intertropical Convergence Zone (ITCZ) where dry Westerlies and moisture-bearing ISM airmasses meet in response to cooling in the North Atlantic results in weaker ISM precipitation in the northern Indian Ocean. However, they attribute transmission of the signal to reorganization of the Hadley cell in response to slowdown in thermohaline circulation and conclude that this is the dominant control on the strength of the ISM regardless of the background glacial state.

Modern observations indicate that direct heating of the Tibetan Plateau results in greater ISM-related precipitation on an annual basis. The increase in rainfall amount is correlated to interannual moist static energy (Rajagopalan & Molnar, 2013) and is primarily due to an increase in precipitation during early and late

monsoon season. In addition, until disrupted by global warming, increased snowfall on the Tibetan Plateau correlated with a later and weaker ISM (Liu et al., 2004; Senan et al., 2016; Vernekar et al., 1995; Zhang et al., 2019).

Although the EAM and the ISM are dynamically connected, they respond to different forcing mechanisms (Wang et al., 2001, 2017). For example, B. Wang et al. (2003) found that variations associated with El Niño-Southern Oscillation (ENSO) lead to greater changes in low-level flow over the South China Sea than over the Arabian Sea, suggesting that the EAM is more sensitive to variations associated with ENSO than the ISM. The history and forcing mechanisms controlling the EAM are relatively well-established from records on the Chinese Loess Plateau (CLP). In the EAM domain, orbital cyclicity related to eccentricity (~100 and 400 kyr cycles), obliquity (~40 kyr cycles), and precession (19 and 23 kyr cycles) are noted in paleosol-loess deposits on the CLP (e.g., An et al., 2001; Clemens et al., 2008; Guo et al., 2002; Heitmann et al., 2017; Li et al., 2017; Nie et al., 2014; Sun & An, 2005), in cave stalagmites in southern China (e.g., Cai et al., 2015; Cheng et al., 2016; Yuan et al., 2004), as well as in marine records (e.g., Clemens et al., 2008; Lisiecki & Raymo, 2005).

In addition to the role orbital forcing plays in monsoon circulation, changes in global ice-volume are also thought to influence the strength of the AMS during the late Miocene (Nie et al., 2017). For example, an increase in Southern Hemisphere ice volume has been linked to stronger AMS (including both ISM and EAM systems) circulation in both Cenozoic proxy records and climate models (An et al., 2011; Ao et al., 2016; Heitmann et al., 2017). In contrast, an increase in Northern Hemisphere ice volume is thought to weaken the AMS in response to a weakened land-sea pressure gradient (Heitmann et al., 2017, and references therein), a cooler North Atlantic, and possibly more snow cover on the Tibetan Plateau and in central Asia (see above).

Lacustrine sediments in the southern Tibetan Plateau provide a sensitive record of ISM strengthening and weakening (Fontes et al., 1996; Morrill et al., 2006; Wang et al., 2002; Zhu et al., 2009). The primary controls on the stable isotopic composition of lacustrine carbonate ($\delta^{18}O_{carb}$ and $\delta^{13}C_{carb}$) records from Tibetan Plateau lakes are the isotopic composition of precipitation (Gao et al., 2014), changes in the precipitation/evaporation (P/E, or inflow/evaporation [I/E] ratio, Cui et al., 2017; Yuan et al., 2011), and changes in basin hydrology (Saylor et al., 2010a; Shi et al., 2014). The primary mechanism driving precipitation $\delta^{18}O$ and δD values ($\delta^{18}O_p$ and δD_p, respectively) toward extremely negative values is Rayleigh distillation during orographic lifting over the southern Himalayan front (Garzione et al., 2000; Quade et al., 2011; Rowley, 2007). General circulation models indicate that fluctuations in Asian monsoon intensity play a secondary role in controlling $\delta^{18}O_p$ values, with increases in precipitation amount correlating with more negative $\delta^{18}O_p$ and δD_p values (Vuille et al., 2005). A competing mechanism controlling the stable isotopic composition of lake water is evaporative enrichment of heavy isotopes in standing lake water, particularly in terminal lake basins (Li & Ku, 1997; Talbot, 1990). Changes in the isotopic composition of lake water are archived in lacustrine organic material (Günther et al., 2015) and carbonate (Fontes et al., 1996). Hence, an increase (decrease) in the precipitation amount or the P/E ratio leads to an increase (decrease) in lake level and lower (higher) $\delta^{18}O_{carb}$ values of lake water. Similarly, long residence times in a closed-lake setting would result in elevated lake water $\delta^{18}O_{carb}$ values, while short residence times in through-flowing fluvial settings would result in low $\delta^{18}O_{carb}$ values (Li & Ku, 1997). Hence, the isotopic composition of authigenic carbonates in Tibetan Plateau lakes is controlled primarily by a combination of changes in basin hydrology and moisture delivery by the ISM.

In Pleistocene–Holocene records from the southern Tibetan Plateau, ISM strengthening is associated with lake expansion and a rise in base level whereas weakening of the monsoon is correlated with base-level fall and lake contraction (Gasse et al., 1996; Hudson & Quade, 2013). Late Miocene–Pliocene climate and environmental change have been documented primarily at low elevations adjacent to the Tibetan Plateau (Molnar, 2005, and references therein). Few long-term climate records have been acquired from the plateau itself. As a result, conclusions about environmental change on the plateau are largely based on indirect evidence. We combine the stable isotope, grain size, and depositional environment record from the Zhada Basin, which is an exceptionally high-resolution and well-dated lacustrine basin on the southwestern Tibetan Plateau, and provides a unique multi-proxy record of past changes in ISM evolution on orbital time scales.

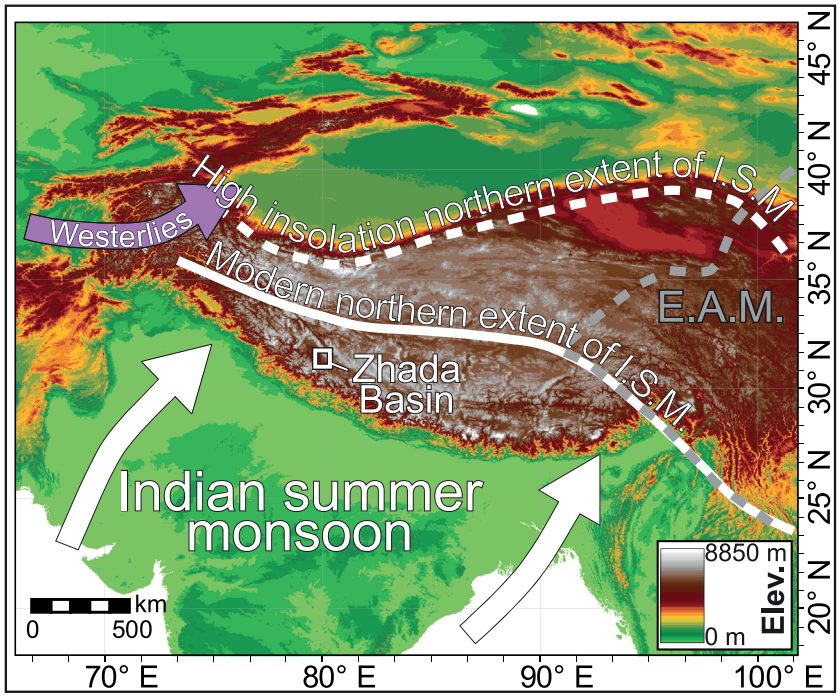

Figure 1. Digital elevation model of Tibetan Plateau showing location of Zhada Basin relative to major climate systems. Modern (low insolation) and early Holocene (high insolation) ISM extent from Araguas-Araguas et al. (1998),Tian et al. (2001), and Winkler & Wang (1993). E.A.M. = East Asian Monsoon; I.S.M. = Indian Summer Monsoon. Modified from Saylor et al. (2016).

1.1. Geologic Setting and Climate

The Zhada Basin is a high-elevation (3.5–4.5 km) hinterland basin just north of the Himalayan ridge crest in the western part of the orogen (~32°N, 82°E; Figure 1) (Saylor et al., 2009). The Zhada Formation consists of >800 m of undeformed fluvial, lacustrine, eolian, and alluvial fan deposits (Kempf et al., 2009; Saylor et al., 2010a). It is capped by a geomorphic surface that extends across the basin and marks the maximum extent of sediment aggradation prior to integration of the modern Sutlej River drainage network (Saylor et al., 2010a). Post-depositional incision by the Sutlej River exposed the Zhada Formation, providing access to an unparalleled paleoclimatic record. Magnetostratigraphy and biostratigraphy constrain the age of the Zhada Formation to ~9.2–<1 Ma (Saylor et al., 2009). The Zhada Basin has been at high elevations since at least the late Miocene, indicating that variations in $\delta^{18}O_{carb}$ are attributable to one of the mechanisms outlined above rather than to elevation gain (Huntington et al., 2015; Saylor et al., 2009).

The climate of the southwestern Tibetan Plateau is dominated by the ISM (Araguas-Araguas et al., 1998; Conroy & Overpeck, 2011; Li & Garzione, 2017; Tian et al., 2001; Yu et al., 2007) (Figure 1). The Zhada Basin's proximity to the northernmost extent of modern (i.e., low insolation) ISM precipitation makes it an ideal location to document long-term changes in ISM strength (Yao et al., 2013), as northward or southward migration of the ITCZ is expected to be expressed as lake expansion or contraction and attendant changes in lacustrine carbonate stable isotope composition at this location.

2. Methods

2.1. Sample Preparation

We undertook stable isotope and grain size analysis on sediment samples collected from the South Zhada stratigraphic section (Figure 2) of Saylor et al. (2010a). Prior to stable isotope analysis, sediment samples were crushed with a mortar and pestle and treated with 30% H_2O_2 to remove organic material. Stable isotopes of oxygen and carbon from 747 bulk carbonate samples (expressed as $\delta^{18}O_{carb}$ and $\delta^{13}C_{carb}$ in units ‰ and referenced to Vienna Pee Dee Belemnite [VPDB]; Table S1 of the supplementary information)

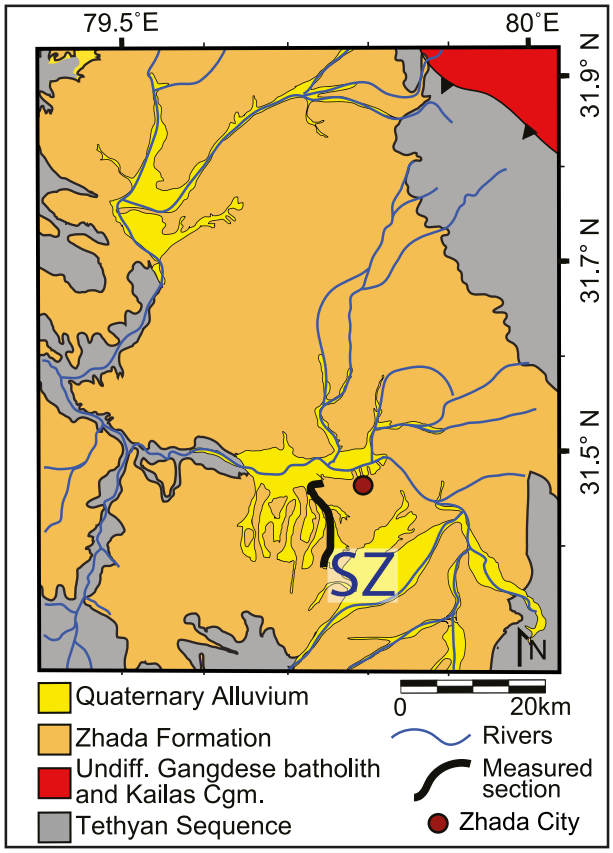

Figure 2. Regional map of the Zhada Basin showing the location of the stratigraphic section from which data are reported (SZ). Cgm. = conglomerate; SZ = South Zhada; Undiff. = undifferentiated; Modified from Saylor et al. (2016).

were measured; 573 samples were analyzed using a Finnigan MAT 252 gas-source, isotope ratio mass spectrometer at the University of Texas at Austin, and 174 samples were measured using a Thermo Scientific Gasbench-Delta V at the University of Texas Arlington. Sample ages were determined by linear interpolation between paleomagnetic ties of the preferred magnetostratigraphic correlation of Saylor et al. (2009). The magnetostragraphic correlation of Saylor et al. (2009) is based on data from 91 sites (Figure S1), as well as independent temporal anchors based on biostratigraphy. See Saylor et al. (2009) for discussion of alternative possible age models.

In order to test the potential effect of contamination by detrital carbonate or large shell fragments and to assess whether there was diagenetic resetting of the authigenic $\delta^{18}O_{carb}$ and $\delta^{13}C_{carb}$ values, we performed the following analyses on subsets of the total 747 samples. To assess the impact of detrital carbonate, we selected 20 samples from a variety of depositional environments, sieved them to 45 μm, and reanalyzed the stable isotope composition of the fine-grained fraction. We also applied petrographic analysis to 56 samples from all depositional environments to evaluate the effect of diagenesis on the isotopic record. Detailed descriptions of each lithofacies association identified with petrography can be found in Table S7.

For grain size analysis, 413 bulk samples were disaggregated by soaking in a solution of deionized water and sodium hexametaphosphate for at least 3 days. Samples were subsequently defloculated in an ultrasonic bath for 4 hr. Samples were removed from the ultrasonic bath and analyzed in a CILAS 1190 particle-size analyzer at the University of Houston. The grain size data for each sample are reported in Table S2. A detailed comparison of lithostratigraphy, the stable isotope record, and mean grain size data are reported in Figure S2.

2.2. Sampling Frequency

Following the work of Saylor et al. (2016), the Zhada Basin stratigraphy is separated into three intervals (A, B, and C) based on differences in mean $\delta^{18}O_{carb}$ values (Figure 3). The upper portion of interval B (4.2–3.5 Ma; 370–510 m) was isolated for further analysis based on differences in sampling frequency (Figure 4). Samples for stable isotope analysis were analyzed at ~1.8 m intervals from 40 to 220 m (interval A; 9.0–6.0 Ma), at ~ 0.8 m intervals from 225 to 510 m (interval B; 6.0–3.5 Ma), and at ~0.6 m intervals from 526 to 635 m (interval C; 3.5–2.3 Ma) of the Zhada Formation. This corresponds to a sampling frequency of 1 sample/29 kyr for interval A, 1 sample/7 kyr for interval B, and 1 sample/5.5 kyr for interval C. The sampling resolution of interval B varies from ~1.3 m intervals from 225 to 370 m (lower B; 6.0–4.3 Ma) to ~0.5 m intervals from 370 to 510 m (upper B; 4.2–3.5 Ma). This corresponds to a sampling frequency of 1 sample/14 kyr for lower B and 1 sample/2.8 kyr for upper B.

Samples for grain size analysis were analyzed at ~1.8 m intervals from 40 to 220 m (interval A; 9.0–6.0 Ma), at ~2.5 m intervals from 225 to 510 m (interval B; 6.0–3.5 Ma), and at ~2.0 m intervals from 526 to 635 m (interval C; 3.5–2.3 Ma) of the Zhada Formation. This corresponds to a sampling frequency of 1 sample/29 kyr for interval A, 1 sample/21 kyr for interval B, and 1 sample/20 kyr for interval C.

2.3. Spectral Analysis

Spectral analysis was performed to determine the dominant frequencies present in the Zhada Basin's $\delta^{18}O_{carb}$ record. Prior to spectral analysis, each interval (A, B, and C) was detrended by removing the mean and dividing by the standard deviation for that interval to allow comparison between each interval. We applied REDFIT spectral analysis (Schulz & Mudelsee, 2002) using PAST v3.0 software (Hammer et al., 2001) to conduct time series analysis directly on the unevenly spaced data from each interval (A, B, upper B, and

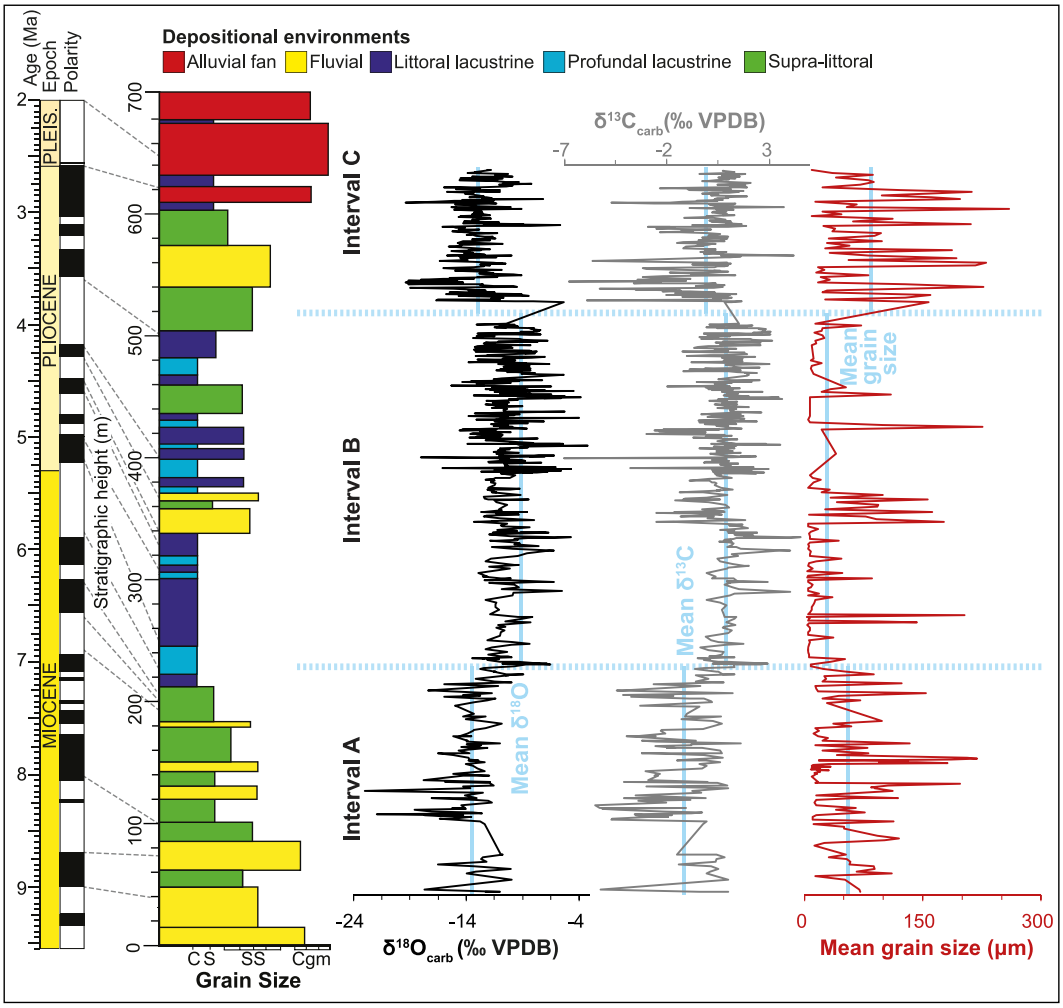

Figure 3. South Zhada stratigraphic section and preferred magnetostratigraphic correlation of Saylor et al. (2009) to the geomagnetic polarity time scale of Lourens et al. (2004). Lithology, $\delta^{18}O_{carb}$, $\delta^{13}C_{carb}$, and mean grain size values from the Zhada stratigraphic section all show systematic changes between intervals A and B and between intervals B and C. Vertical blue lines indicate mean δ values or grain size for each interval. C = clay; S = silt; SS = sandstone; Cgm = conglomerate. All $\delta^{18}O_{carb}$ and $\delta^{13}C_{carb}$ values are expressed in units ‰ and referenced to Vienna Peedee Belemnite. Stratigraphic column modified from Saylor et al. (2016).

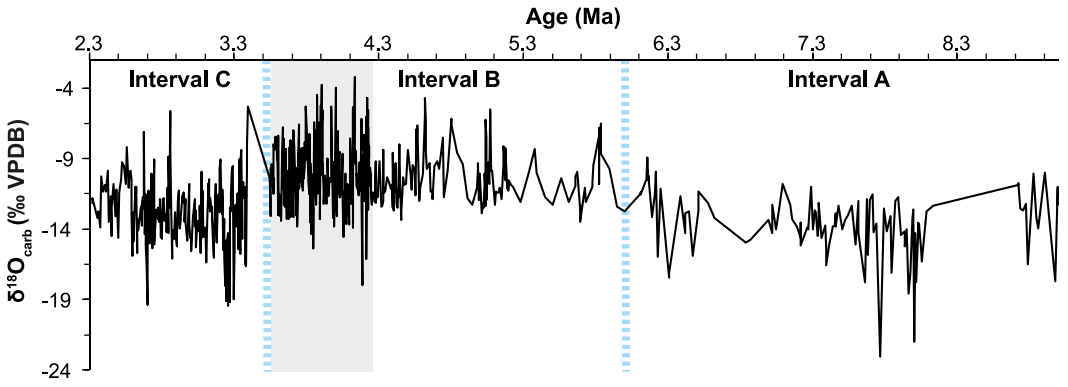

Figure 4. The Zhada Basin's $\delta^{18}O_{carb}$ record versus age (Ma). Gray box indicates the location of interval upper B, shown in Figure 5. $\delta^{18}O_{carb}$ values are expressed in units ‰ and referenced to Vienna Peedee Belemnite.

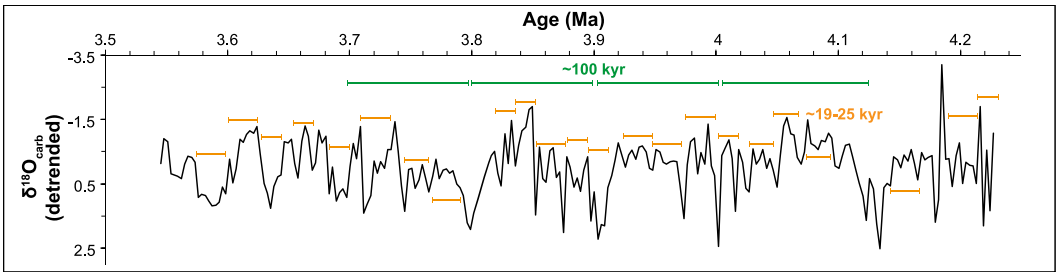

Figure 5. The Zhada Basin's $\delta^{18}O_{carb}$ record (detrended) versus age (Ma) for interval upper B (4.23–3.55 Ma) mimics the cyclicity related to changes in eccentricity (green) and precession (orange).

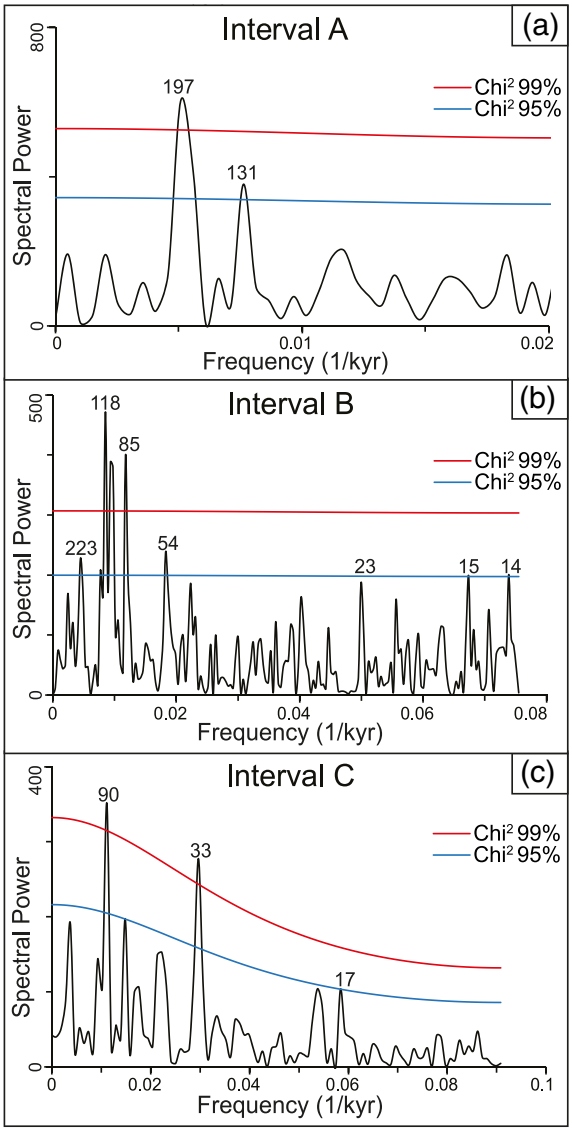

Figure 6. Power spectra plots of the $\delta^{18}O_{carb}$ record across intervals (A, B, and C). (a) Interval A (~9.0–6.15 Ma) lacks orbital cyclicity, (b) Interval B (6.2–3.5 Ma) is dominated by 118 and 85 kyr eccentricity cycles (chi-square 99%), and (c) Interval C (3.5–2.2 Ma) has a prominent 90 kyr cycle (chi square 99%). Red-noise boundaries are estimated as upper 95% (blue) and 99% (red) chi square limits of a fitted AR1 process. Values correspond to cycles per kyr.

C). When applying REDFIT, we selected a Welch window. Red-noise boundaries were estimated as upper 95% and 99% chi square limits of a fitted AR1-process.

2.4. Chronology

Age constraints of Saylor et al. (2009) provided the framework to develop an astronomically tuned age model for interval upper B (4.23–3.55 Ma). The new chronology was generated by correlating the Zhada Basin's $\delta^{18}O_{carb}$ time series to computed variations of daily insolation calculated on 21 June at 35°N (Laskar et al., 2004). We applied a Gaussian band-pass filter centered at 0.05 kyr (20 kyr period) with a 0.01 bandwidth to both the Zhada Basin's $\delta^{18}O_{carb}$ series and to the daily insolation curve. The resulting curves revealed similarity in terms of amplitude, allowing us to refine our time scale (Figure S6). We applied a minimal tuning strategy using 13 tie points to preserve original spectral characteristics and to avoid artificial changes in sedimentation rates (Muller & MacDonald, 2002) (Figure S7). Age tie-points and the calculated sedimentation rate can be found in Tables S5 and S6, respectively. Ages were modified by less than half of a precession cycle (average [mean] absolute difference: 5.5 kyr, standard deviation: 4.3 kyr, maximum difference: 13.2 kyr, minimum difference: 0.23 kyr). Tuning was conducted independent of, and prior to, spectral analysis of the tuned record: the process was not iterative.

2.5. Wavelet Analysis

Wavelet analysis was performed on the tuned $\delta^{18}O_{carb}$ record for interval upper B (4.23–3.55 Ma) (Figures 4 and 5), where our sampling resolution is high enough to resolve precession, obliquity, and eccentricity cycles. Prior to wavelet analysis, we utilized the *linspace* function in MATLAB to convert our unevenly spaced data to an evenly spaced timeseries. Wavelet analysis was performed using the PAST v3.0 software (Hammer et al., 2001) and is based on the methods laid out in Torrence and Compo (1998). The mother wavelet is Morlet, the lag-1 autocorrelation for the red-noise background is 0.5. The evenly spaced time series data for upper B is reported in Table S4.

2.6. Coherence and Cross-Correlation Analysis

In order to evaluate whether the Zhada Basin's $\delta^{18}O_{carb}$ record shares periodicities with insolation, we conducted coherence analysis between the oxygen isotope record from interval upper B and the record of daily insolation (calculated at 35°N, 21 June) using

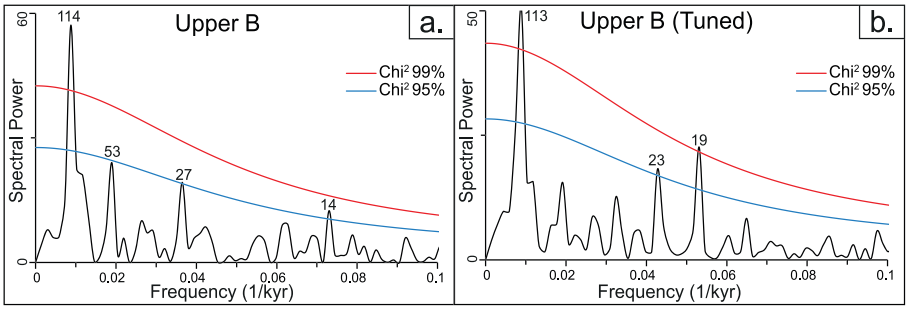

Figure 7. Power spectra plots of both the untuned (a) and tuned (b) $\delta^{18}O_{carb}$ record across interval upper B (4.23–3.55 Ma). Red-noise boundaries are estimated as upper 95% (blue) and 99% (red) chi square limits of a fitted AR1 process. Values correspond to cycles per kyr.

software developed by P. Huybers (http://www.people.fas.harvard.edu/~phuybers/Mfiles/index.html) with a window of 4. To evaluate the phasing between the oxygen isotope record and insolation, we calculated the cross-correlation between the $\delta^{18}O_{carb}$ and insolation records using the MATLAB *xcorr* algorithm. For the coherence and cross-correlation analysis we used the evenly spaced tuned and untuned oxygen isotope record as well as a random time-series, and the insolation record was sampled at the same time-step (1 sample/2.79 kyr) as our record.

3. Results

3.1. Stable Isotope Record

Comparison of mean values from intervals A, B, and C using our more densely sampled data set confirms previously interpreted breaks in the Zhada Formation stratigraphy based on statistically significant changes in mean $\delta^{18}O_{carb}$, $\delta^{13}C_{carb}$, and grain size values (Figure 3). The $\delta^{18}O_{carb}$ values range from −3‰ to −23‰ across the Zhada Formation. There is a positive shift in mean $\delta^{18}O_{carb}$ values shift from −13.5‰ to −10.2‰ across the A-B transition at ~225 m (Student's *t* test *p* value < 3.7E-29). This is followed by a negative shift in mean $\delta^{18}O_{carb}$ values from −10.2‰ to −12.9‰ across the B-C transition at ~525 m (Student's *t* test *p* value < 8.3E-38). The $\delta^{13}C_{carb}$ values range from 4.5‰ to −7‰. There is a positive shift in mean $\delta^{13}C_{carb}$ values from −1.2‰ to 0.9‰ at ~225 m (Student's *t* test *p* value < 1.5E-24). This is followed by a negative shift in mean $\delta^{13}C_{carb}$ values from 0.9‰ to −0.1‰ at ~525 m (Student's *t* test *p* value < 1.9E-14).

The mean grain size values range from 3.5 to 259 μm across the Zhada Formation. There is a decrease in mean grain size values from 56.9 to 28.7 μm across the A-B transition at ~225 m (Student's *t* test *p* value < 1.9E-5). This is followed by an increase in mean values from 28.7 to 85.3 μm across the B-C transition at ~525 m (Student's *t* test *p* value < 4.9E-7).

3.2. Spectral Analysis of $\delta^{18}O_{carb}$ Record

REDFIT spectral analysis reveals a dominant frequency of ~100 kyr cycles from ~6.0–2.2 Ma (Figure 6). Interval A (Figure 6a; 8.1–6.1 Ma; 1 sample/21 kyr) lacks any frequencies consistent with orbital forcing. Interval B (Figure 6b; 6.0–3.5 Ma; 1 sample/7 kyr) includes 118 and 85 kyr period cycles above the 99% confidence limits and cycles with periods of 223, 54, 15, and 14 kyr above the 95% confidence limits. Interval C (Figure 6c; 3.5–2.2 Ma; 1 sample/5.5 kyr) is dominated by 90 and 33 kyr period cycles above the 99% confidence limits and 17 kyr period cycles above the 95% confidence limits.

REDFIT spectral analysis of both the untuned and tuned upper B (Figure 7; 4.23–3.55 Ma; 1 sample/2.8 kyr) reveals prominent ~110 kyr period cycles. The untuned record (Figure 7a) has 114 kyr period cycles above the 99% confidence limits and 53, 27, and 14 kyr period cycles at the 95% confidence limits. In comparison, the tuned record (Figure 7a) shows 113 and 19 kyr period cycles above the 99% confidence limits and 23 kyr period cycles above the 95% confidence limits.

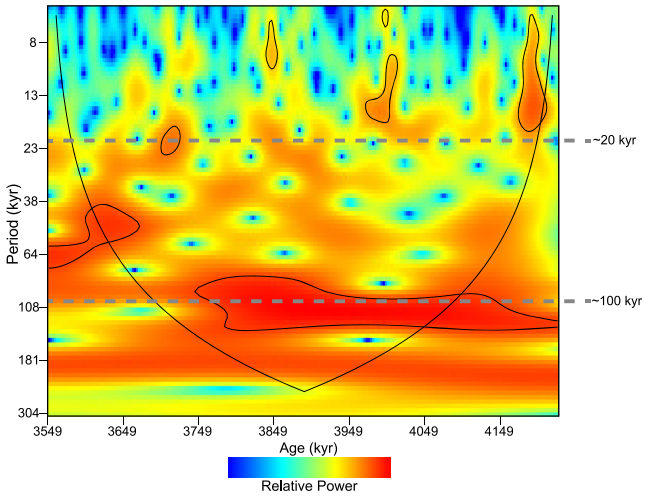

Figure 8. Wavelet transform of the tuned $\delta^{18}O_{carb}$ record across interval upper B. Color scale indicates relative power, which is the normalized wavelet power spectrum (warmer colors indicates larger power). The black contour is the 95% confidence level.

3.3. Wavelet Analysis

Wavelet analysis of the early Pliocene (4.23–3.55 Ma) portion of the record shows the highest relative power at ~100 kyr periods between 4.23 and 3.75 Ma (Figure 8). It also shows punctuated intervals of relatively high power at ~20 kyr periods at ~4.1, 3.95, 3.8 and 3.7 Ma.

3.4. Coherence and Cross-Correlation Analysis

Analysis of the periodicities shared between the tuned upper B $\delta^{18}O_{carb}$ record and insolation (i.e., coherence analysis) reveals the strongest coherence at ~20 kyr periods (Figure 9a). Cross-spectrum analysis indicates that at those frequencies the $\delta^{18}O_{carb}$ record and insolation are anticorrelated at those periods (i.e., they are 180 degrees out of phase, Figure 9b). In comparison, the untuned and random time-series show no coherence at Milankovitch frequencies (Figures 9c and 9e). Cross-correlation analysis indicates that the evenly spaced, tuned $\delta^{18}O_{carb}$ and insolation records are anticorrelated (Figure 10). It also shows that the correlation is strongest at a lag of 0 kyr, followed by a lag of approximately ±20 and

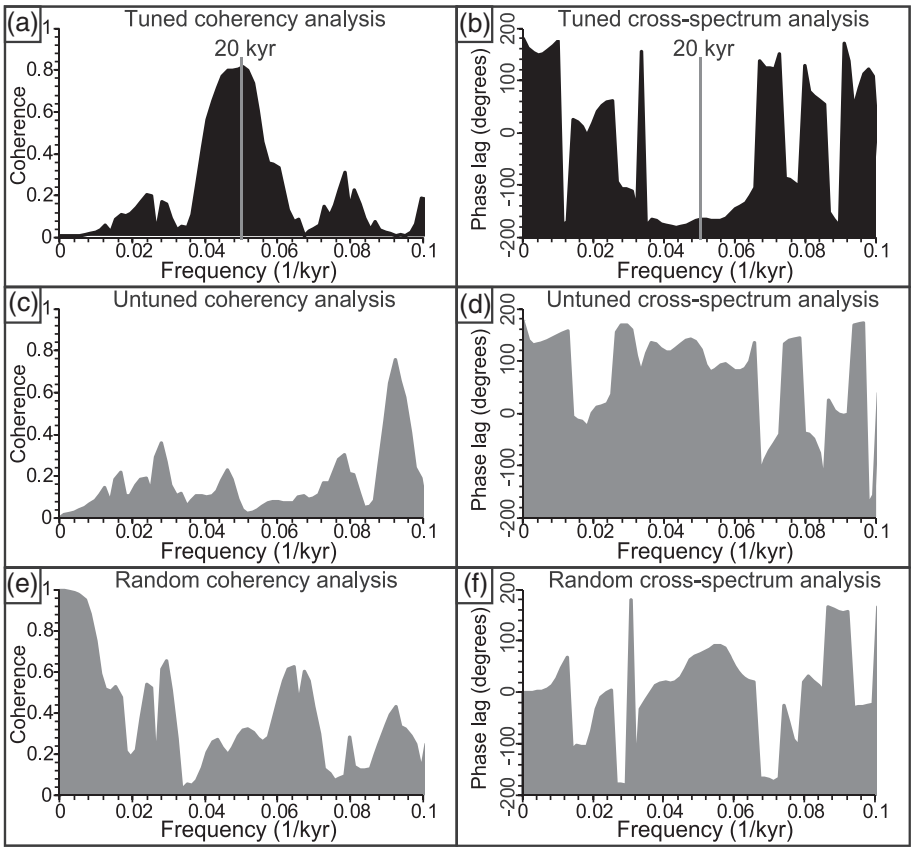

Figure 9. (a) Coherence analysis between the evenly spaced, tuned Zhada Basin $\delta^{18}O_{carb}$ record and daily insolation (21 June, at 35°N) from 4.2 to 3.5 Ma (upper B) confirms that these records share frequencies with ~20 kyr periods. (b) Cross-spectrum analysis between the evenly spaced, tuned Zhada Basin $\delta^{18}O_{carb}$ record and daily insolation from 4.2 to 3.5 Ma (upper B) indicates that at ~20 kyr (i.e., precession) periods shows that their phases are opposite, as predicted if Northern Hemisphere insolation directly drives variability in ISM strength. (c) Coherence and (d) cross-spectrum analysis between the evenly spaced, untuned $\delta^{18}O_{carb}$ record and insolation from 4.2 to 3.5 Ma. (e) Coherence and (f) cross-spectrum analysis between a random time series with the same length and spacing as the Zhada Basin records.

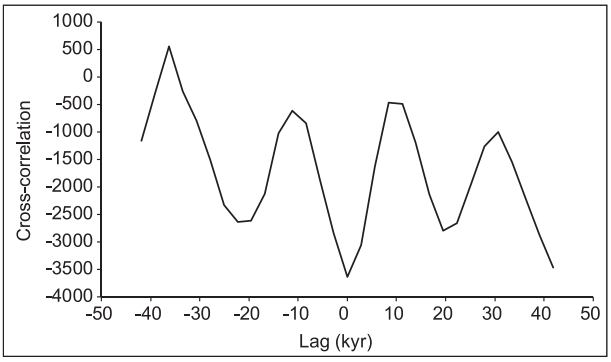

Figure 10. Cross-correlation between the evenly spaced, tuned Zhada Basin $\delta^{18}O_{carb}$ record and the record of daily insolation (21 June, at 35°N) from 4.2 to 3.5 Ma (upper B). Anticorrelation between these records confirms that the ISM strengthens as insolation increases. The absolute value of the correlation maximized at 0, ±20, and ±40 kyr offsets confirms that Northern Hemisphere, rather than Southern Hemisphere, insolation is the primary driver of ISM variability.

±40 kyr. The correlation is lowest at offsets of approximately ±10 and ±30 kyr.

4. Discussion

4.1. Basin Evolution

Changes in $\delta^{18}O_{carb}$, $\delta^{13}C_{carb}$, and the mean grain size record between intervals A, B, and C reflect major basin-wide changes in basin hydrology (Saylor et al., 2016), which are also evident in changes in depositional environments and sequence stratigraphic stacking patterns (Saylor et al., 2010b; Saylor et al., 2013). Low $\delta^{18}O_{carb}$ values from the fluvial facies in interval A (9.0–6.0 Ma) are consistent with unevaporated fluvial water on the southern Tibetan Plateau (Li & Garzione, 2017; Quade et al., 2011; Saylor et al., 2009). Very negative $\delta^{18}O$ values of river water result from Rayleigh distillation during orographic ascent (Garzione et al., 2000; Rowley et al., 2001) and are consistent with modern or greater-than-modern elevation of the late Miocene Zhada Basin (Huntington et al., 2015; Saylor et al., 2009). In addition, the $\delta^{18}O_{carb}$ and $\delta^{13}C_{carb}$ values show little covariance (Interval A: $r^2 = 0.40$; Figure 11), suggesting low water-residence times associated with a through-flow fluvial system (Li & Ku, 1997; Talbot, 1990). High-frequency, non-systematic migration of fluvial depositional environments may have obscured higher frequency climate signals in the record and could account for lack of periodic variability observed in the $\delta^{18}O_{carb}$ values during interval A (Figure 6a).

The increase in mean $\delta^{18}O_{carb}$ and $\delta^{13}C_{carb}$ values, $\delta^{18}O_{carb}$ and $\delta^{13}C_{carb}$ correlation coefficients (Interval B: $r^2 = 0.57$; Figure 11), and the decrease in mean grain size values at ~225 m (6.0 Ma) reflect flooding of the basin and an increase in residence time (Bohacs et al., 2000; Li & Ku, 1997; Talbot, 1990), consistent with the development of a hydraulically closed or balance-filled paleo-Lake Zhada at that time (Saylor et al., 2010b; Saylor et al., 2016). Expansion and contraction of paleo-Lake Zhada are recorded by high-frequency variations in $\delta^{18}O_{carb}$ values and rapid progradation of lake margin lithofacies resulting in juxtaposition of lithofacies representing littoral depositional environments over profundal depositional environments (Saylor et al., 2010b). We interpret these changes as reflecting changes in lake volume associated with hydroclimatic changes driven by strengthening and weakening of the ISM (Saylor et al., 2010b). Previous isotopic analysis of modern surface waters in the area indicates that the $\delta^{18}O$ values of lacustrine waters are elevated due to evaporation (Li & Garzione, 2017; Quade et al., 2011; Saylor et al., 2009). A similar pattern is also recognized in Miocene–Pliocene carbonates: $\delta^{18}O$ values of lacustrine mollusks are evaporatively enriched in ^{18}O (Saylor et al., 2009). Evidence for evaporative environmental conditions throughout this time agrees with the occurrence of gypsum and mud cracks identified in outcrop (Saylor et al., 2009) and the occurrence of oxidized horizons in carbonaceous mudstones identified with petrography (Figures S3E and S3F).

The decrease in $\delta^{18}O_{carb}$ and $\delta^{13}C_{carb}$ covariance ($r^2 = 0.42$; Figure 11), mean $\delta^{18}O_{carb}$ and $\delta^{13}C_{carb}$ values, and increase in mean grain size between interval B and C reflects a decrease in lake size such that the sampling location was occupied by lake-margin depositional environments (Saylor et al., 2016). Saylor et al. (2016) attribute this transition to a drop in base level, which they attributed to a long-term decrease in ISM strength and an increase in arid conditions (Su et al., 2016). Interval C (3.5–2.2 Ma) is characterized by progradation of deltaic depositional environments with intermittent lacustrine carbonate deposition (Saylor et al., 2010b). The decrease in base level occurred synchronously with or slightly after an increase in drought-tolerant flora observed in the pollen record of the Zhada Formation (Wu et al., 2014; Zhu et al., 2007). The presence of salinity-tolerant ostracod species in interval C also points to continued under- or balance-filled conditions and an increase in the evaporative conditions throughout this time (Zhu et al., 2007). Comparison between $\delta^{13}C_{carb}$, $\delta^{18}O_{carb}$, and mean grain size values against lithofacies associations reveals that variations in the records are dependent on depositional environments, but this relationship alone cannot account for the variations that are observed within each environment (Figure 12).

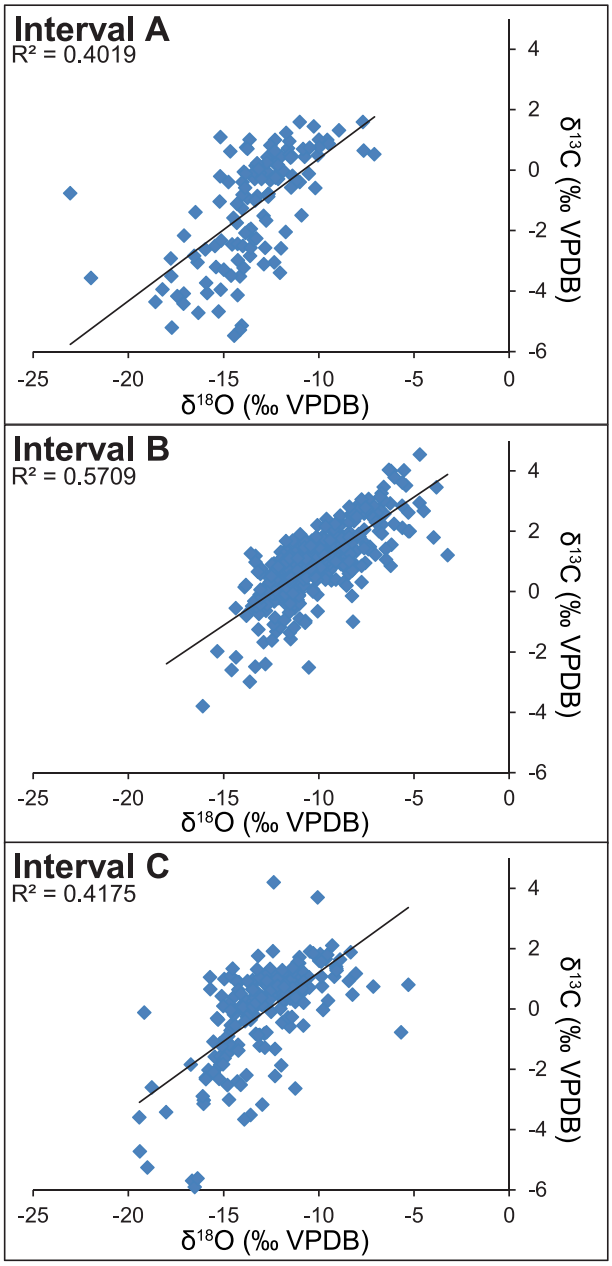

Figure 11. $\delta^{18}O_{carb}$ and $\delta^{13}C_{carb}$ cross-plots and correlation coefficients for intervals A, B, and C from the Zhada stratigraphic section. Correlation coefficients increase in interval B during a period dominated by lacustrine deposition.

4.2. Regional Controls on Long-Term ISM Intensity

The ISM is thought to weaken in response to cooler tropical Indian Ocean temperatures (Terray et al., 2003; Wang et al., 2005). Cane and Molnar (2001) suggested that closure of the Indonesian seaway may have changed the source of flow through the seaway from warm south Pacific water to cold north Pacific water, cooling the Indian Ocean. However, the shift in mean $\delta^{18}O_{carb}$ values at the transition between interval B and C (at 3.4–3.5 Ma) (Figure 13a) predates significant cooling in the Indian Ocean (at ~3.3 Ma) (Figure 13c), suggesting that the closure of the Indonesian seaway may have had less of an influence on weakening of the ISM than previously suggested (Karas et al., 2009; Saylor et al., 2016). This conclusion is tempered by the fact that only a minor revision of either chronology would be needed to synchronize these events. Nevertheless, as currently documented these records suggest that cooling Indian Ocean temperatures and SSTs were not the dominant driver of long-term ISM weakening on the southwestern Tibetan Plateau.

Comparison of the $\delta^{18}O_{carb}$ record from the Zhada Basin to SST records from the Arabian Sea and eastern Pacific Ocean suggests that neither of them is responsible for the abrupt change in Zhada Basin $\delta^{18}O_{carb}$ values at 3.4–3.5 Ma. Despite the cooling trend observed in the SST records from the Arabian Sea (Figure 13g) and from the eastern Pacific Ocean (Figure 13h), mean $\delta^{18}O_{carb}$ values from the Zhada Basin remain constant until the decrease at 3.4–3.5 Ma (Interval C) (Figure 13a). Although the observed trend is incompatible with a linear relationship between SST in the Arabian Sea or eastern Pacific Ocean and the $\delta^{18}O_{carb}$ record in Zhada Basin, it does not preclude a threshold response to changing SSTs.

The major decrease in $\delta^{18}O_{carb}$ values in Interval C has been previously attributed to an onset of arid conditions (Kempf et al., 2009; Saylor et al., 2016; Zhu et al., 2007) due to a tectonically driven decrease in elevations and coeval weakening of ISM and strengthening of EAM circulation (Saylor et al., 2016). A decrease in elevation since ~3.7 Ma may have been sufficient enough to allow for a decrease in ISM circulation due to decreased thermal forcing of an elevated landmass (Huntington et al., 2015; Tang et al., 2013). Nonetheless, the presence of 90 and 17 kyr cycles in interval C (Figure 6c) suggests that orbital forcing of insolation-variations continued to play a fundamental role in environmental change on the southern Tibetan Plateau throughout this time.

4.3. Orbital Control on the $\delta^{18}O_{carb}$ Record

Carbon isotopes in lacustrine settings are impacted by multiple factors including lacustrine biological activity and atmospheric $\delta^{13}C$ and are not as directly affected by aridity and evaporation as $\delta^{18}O_{carb}$ (Li et al., 2000). As a result, we found that high-frequency climate cycles are not as well expressed in the carbon isotope record as in the oxygen isotope record (Figure 14). Our discussion below therefore focuses on the oxygen isotope record.

Spectral analysis of interval the $\delta^{18}O_{carb}$ record across the most densely sampled portion of interval A (Figure 6a; ~100 to ~200 m) reveals no orbital periods in the stable isotope record from ~9.0 to ~6.1 Ma. This may reflect either the non-periodic nature of fluvial migration or the low-sampling resolution for this interval. Eccentricity (~100 kyr) and precession (~20 kyr) cycles are recorded in interval B (Figure 6b; 6.0–3.5 Ma; 1 sample/7 kyr) and interval C (Figure 6c; 3.5–2.2 Ma; 1 sample/5.5 kyr), suggesting that

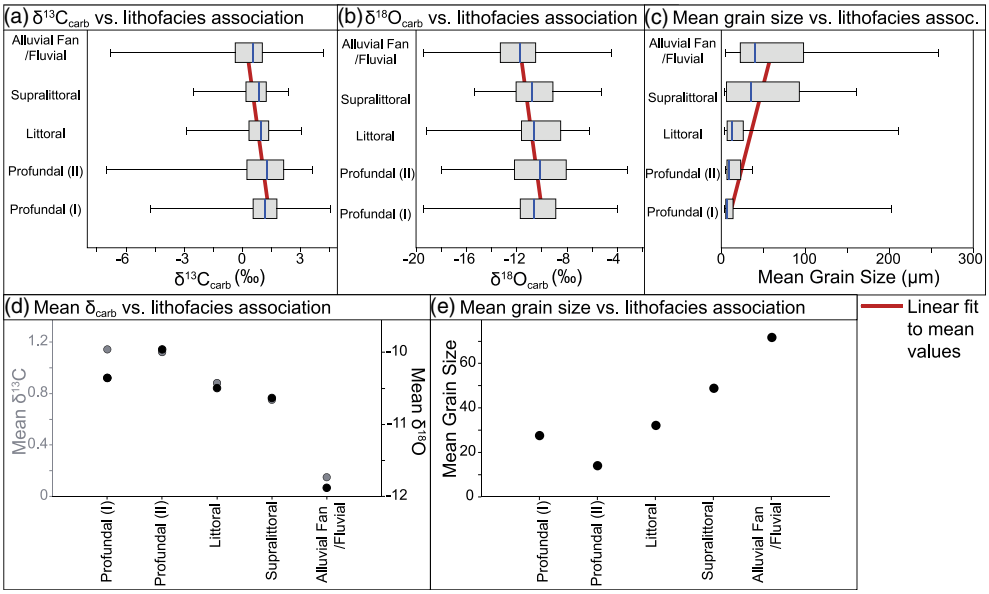

Figure 12. Comparison between $\delta^{13}C_{carb}$, $\delta^{18}O_{carb}$, and mean grain size values against lithofacies associations highlights the variation within each lithofacies association. **(a–c)** Box plots of the $\delta^{13}C_{carb}$ **(a)**, $\delta^{18}O_{carb}$ **(b)**, and mean grain size **(c)** record against lithofacies associations. Box plots illustrate the 25–75% quartiles with the shaded box, the blue line represents the median value, and the minimum (left of blue line) and maximum values (right of blue line) are shown by the short horizontal lines ("whiskers"). The red line represents a linear fit to mean values. **(d)** Mean $\delta^{13}C_{carb}$, $\delta^{18}O_{carb}$, and grain size **(e)** values are plotted against lithofacies associations to further highlight the variability within each lithofacies association. Lithofacies associations are from Saylor et al. (2010b), where profundal (I) and (II) lithofacies associations are defined based on the absence or presence of terrigenous clastic or biologic material, respectively.

orbital cycles are recorded in the Zhada Formation. It is important to note that the Nyquist frequency (half the sampling rate) determines the shortest periodicity that can be resolved in a time-series. However, the sampling rate should be 4–5 times the Nyquist frequency and thus on the order of 1 sample/4 kyr or less to detect a precession cycle (e.g., Luo et al., 2018; Ruddiman, 2001). The Zhada Basin's record for upper interval B satisfies this requirement with a mean sampling resolution of 2.8 kyr.

Spectral analysis of both the untuned and tuned time-series from the upper B interval (4.23–3.55 Ma) yields eccentricity (~100 kyr) and precession (~20 kyr) cycles (Figures 7a and 7b). Comparing the results of our tuned 4.23–3.55 Ma record to our untuned record reveals that tuning did not introduce any artifacts in our data. Tuning interval upper B had no effect on the ~100 kyr cycles. It removed the 53 kyr cycle. However, it shifted and amplified the 19 and 23 kyr precession cycles. Wavelet analysis (Figure 8) of the tuned record confirms the dominance of eccentricity (~100 kyr) and precession cycles throughout 4.23–3.55 Ma. In addition, wavelet analysis (Figure 8) reveals that the eccentricity cycle is much stronger than the precession cycle. We conclude that the ~100 and ~20 kyr cycles are robust, but that the ~50 kyr cycle is likely an artifact.

Variations in the Zhada Basin's $\delta^{18}O_{carb}$ record for the interval upper B (4.23–3.55 Ma; Figure 5) reveal that 20 kyr cycles (indicated by orange bars in Figure 5) are present throughout the time-series but are masked because they are bundled in to 100 kyr cycles (indicated by green bars in Figure 5) which have a greater amplitude than any of the 20 kyr cycles of which they are comprised. We therefore attribute the high spectral power 100 kyr cycles observed in the spectral and wavelet analysis (Figures 6 and 8) to the bundling of 4–5 precession cycles (Huybers, 2011; Huybers & Wunsch, 2005; Liu et al., 2008; Nie et al., 2017). Alternatively, the weaker 20 kyr cycles may be biased due to our age model. Applying linear interpolation to our unevenly spaced data set may have weakened the power of short cycles such as precession (Luo et al., 2018). The Zhada record is interpreted to reflect a clipped response to daily insolation, which can intensify the power of 100 kyr cycles (Nie, 2018). Although 100 kyr cycles dominate our statistical analyses, we refrain from

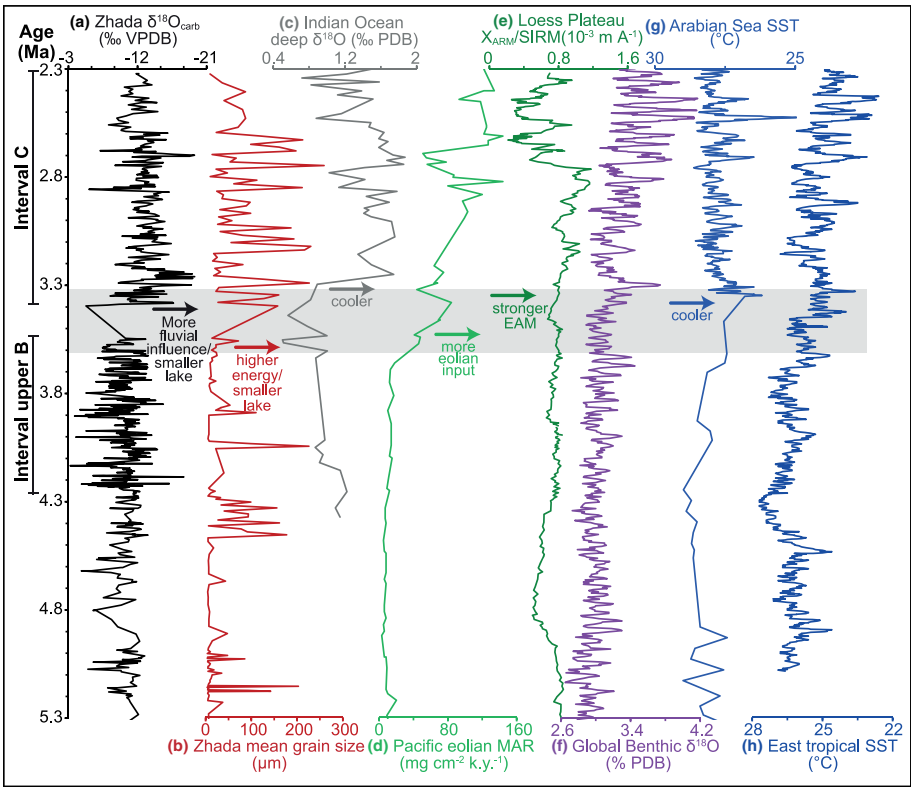

Figure 13. Comparison of the Zhada Basin's $\delta^{18}O_{carb}$ **(a)** and mean grain size **(b)** record to the Indian Ocean deep foraminifera $\delta^{18}O$ values (Karas et al., 2009) **(c)**, Pacific eolian mass accumulation at Ocean Drilling Program Site 885/886 (Rea et al., 1998) **(d)**, the ratio of anhysteretic remnant magnetization susceptibility to saturated isothermal remnant magnetization (X_{ARM}/SIRM), a proxy for EAM strength on the Loess Plateau (Nie et al., 2014) **(e)**, global benthic $\delta^{18}O$ values (Lisiecki & Raymo, 2005) **(f)**, and Sea Surface Temperatures at site 722 in the Arabian Sea (pre 3.25 Ma from Huang et al., 2007, and post 3.25 Ma from Herbert et al., 2010) **(g)**, and from the eastern Pacific Ocean (Lawrence et al., 2006) **(h)**.

assigning the 100 kyr cycle directly to eccentricity because eccentricity has a smaller effect on insolation than precession (Imbrie et al., 1993).

The prominent 100 kyr $\delta^{18}O_{carb}$ cycles throughout 4.23–3.55 Ma differ markedly from the characteristic saw-toothed shape of late Pleistocene glacial cycles (Figure 13f). The Zhada $\delta^{18}O_{carb}$ cycles exhibit sharp increases and decreases that are fairly symmetrical (Figure 5), indicating that different climate dynamics drove these changes. However, an increase in global benthic $\delta^{18}O$ values at ~3.44 Ma (Figure 13f) occurs coeval with the decrease in mean $\delta^{18}O_{carb}$ values from the Zhada Basin (Figure 13a). This relationship may indicate a link between the initiation of glacial–interglacial cycles and environmental change at high-elevations as previously suggested by Saylor et al. (2016).

4.4. Relationship Between ISM and Northern Hemisphere Insolation

Strong coherence between the tuned oxygen isotope record and the record of Northern Hemisphere insolation in the precession band (Figure 9a) suggests that ISM strength is directly driven by Northern Hemisphere insolation. Furthermore, as discussed in section 1.1 above, if greater Northern Hemisphere insolation drives a stronger ISM, higher insolation values should correspond to lower $\delta^{18}O_{carb}$ values in Zhada Basin (i.e., the two records should be anticorrelated). This is confirmed by cross-correlation analysis, which indicates that the $\delta^{18}O_{carb}$ and insolation records are anticorrelated as predicted if insolation directly drives monsoon strength. It also indicates that decreases in $\delta^{18}O_{carb}$ (i.e., strengthening of the ISM) is most strongly correlated with Northern Hemisphere insolation maxima, whereas the ISM is weakest at insolation minima. These observations are consistent with a Northern Hemisphere, rather than Southern Hemisphere driver for ISM strength. Climate models have long attributed monsoon variations on orbital time scales to

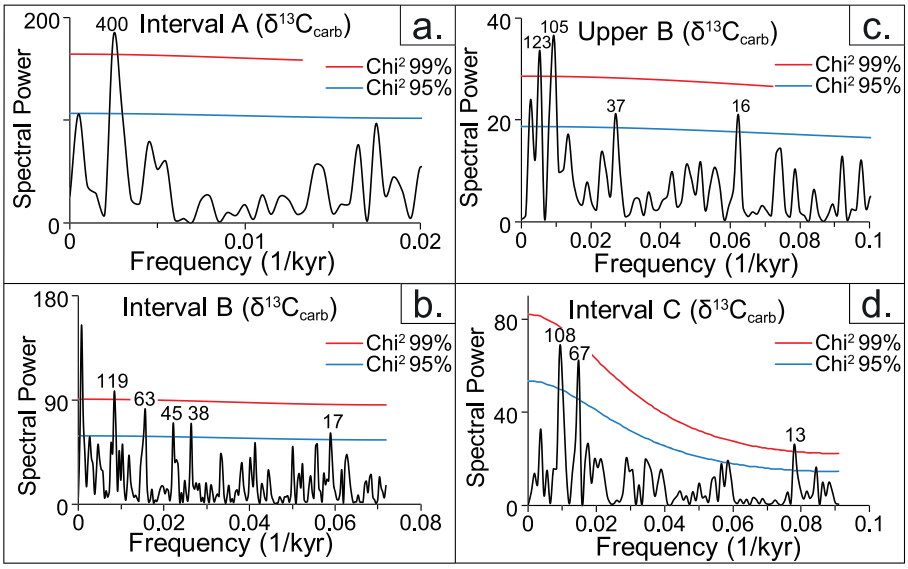

Figure 14. Power spectra plots of the $\delta^{13}C_{carb}$ record across intervals A, B, upper B, and C. Red-noise boundaries are estimated as upper 95% (blue) and 99% (red) chi square limits of a fitted AR1 process. Values correspond to cycles per kyr.

changes in low-latitude summer insolation, which is dominated by precession cycles (Battisti et al., 2014; Kutzbach, 1981; Kutzbach et al., 2008; Liu et al., 2014; Merlis et al., 2013; Tiedemann et al., 1994; Xinzhou et al., 2017). Increasing summer insolation decreases atmospheric pressure over central Asia and strengthens summer monsoonal circulation (Mohtadi et al., 2014). The Zhada Basin's $\delta^{18}O_{carb}$ record suggests that changes in daily insolation have been driving changes in the ISM since at least the late Miocene (~6.0 Ma). In contrast to the work of Clemens et al. (1991), we do not find significant power in the obliquity band or coherence with insolation at obliquity frequencies. This may be the result of changing monsoon dynamics prior to (this study) or after Northern Hemisphere Glaciation (Clemens et al., 1991).

4.5. Comparison of ISM and EAM Forcing Mechanisms

The lack of obliquity signal in the Zhada Basin's $\delta^{18}O_{carb}$ record is consistent with our interpretation that high-frequency variation is controlled by direct irradiative heating of the plateau due to changes in daily insolation, which is dominated by 19 and 23 kyr periodicities. However, Miocene–Pleistocene records of the EAM found a direct link between variations in monsoon precipitation and obliquity (41 kyr) forcing (Heitmann et al., 2017; Li et al., 2017). Heitmann et al. (2017) attribute changes in EAM circulation to variations in the cross-equatorial pressure gradient. The lack of obliquity (41 kyr) cycles in the Zhada record suggests that the ISM and EAM respond to different forcing mechanisms.

5. Conclusions

This research provides the first high-resolution, long-term record of environmental change from the late Miocene–Pleistocene Zhada Basin, southwestern Tibetan Plateau. High-resolution isotopic and grain size data, coupled with petrology and sedimentology of the Zhada Formation, are consistent with previously interpreted breaks in the Zhada Formation stratigraphy at ~6.0 and ~3.5 Ma attributable to tectonically driven formation of a hydraulically closed or balance-filled paleo-Lake Zhada and a decrease in ISM strength, respectively. Basin closure is indicated by an increase in mean $\delta^{18}O_{carb}$ and $\delta^{13}C_{carb}$ values, an increase in $\delta^{18}O_{carb}$ and $\delta^{13}C_{carb}$ correlation coefficients, and a decrease in mean grain size at ~6.0 Ma. An increase in mean-grain size and a decrease in mean $\delta^{18}O_{carb}$ and $\delta^{13}C_{carb}$ values at 3.5 Ma is attributed to a drop in base level due to a long-term decrease in ISM strength and associated increase in aridity.

High-frequency variations in the $\delta^{18}O_{carb}$ values point to cyclical expansion and contraction of a large paleo-lake attributable to changes in precipitation/evaporation due to strengthening and weakening of the ISM. Petrographic analysis reveals that the mean $\delta^{18}O_{carb}$ values from each lithofacies association are

consistent with what is expected from each depositional environment. Furthermore, we found no relationship between samples that contain evidence of detrital input and the $\delta^{18}O_{carb}$ or $\delta^{13}C_{carb}$ values.

Frequency analysis of the stable isotope record reveals that the Zhada Basin's $\delta^{18}O_{carb}$ record is likely dominated by ~100 kyr cycles from 6.0 to 2.2 Ma, with ~20 kyr cycles present but at lower power. The appearance of high-frequency cycles predates the onset of Northern Hemisphere glaciation indicating either that glaciation initiated earlier on the high-elevation Tibetan Plateau or that glacial expansion and contraction is not the primary control of ISM strength. Tuning the record from 4.23 to 3.55 Ma enhances ~20 kyr cycles while subduing non-Milankovitch frequencies. Wavelet analysis of the Zhada Basin's tuned record spanning 4.23–3.55 Ma reveals strong 100 kyr eccentricity and 20 kyr precession cycles suggesting that insolation-driven climate change drove high-frequency environmental changes in southern Tibet. The 100 and 20 kyr periodicities observed in the Zhada record are interpreted to represent a likely clipped response to summer insolation forcing, which has been shown to be largely an eccentricity-modulated precession signal. Coherence analysis shows strong coherence between the isotopic record and the summer record of insolation at precession frequencies. The record from Zhada Basin suggests that direct radiative heating of the high-elevation southern Tibetan Plateau has been the dominant control on high-frequency environmental change since the late Miocene. This also implies that the high-elevation Tibetan Plateau provides a link between high-frequency environmental change and insolation.

Data Availability Statement

Supporting figures and all data generated in this study are included in the @Supporting Information files. The oxygen and carbon isotope record and grain size data are available online (https://www.ncdc.noaa.gov/paleo/study/29210).

Acknowledgments

This work was supported by grants from the National Science Foundation (grant EAR-1226984), the University of Houston (New Faculty Grants), the University of British Columbia, and the American Association of Petroleum Geologists Grants-in-Aid. The authors gratefully acknowledge input from three anonymous reviewers and Associate Editor Stephen Barker for their comments and criticisms which helped to clarify and hone this paper.

References

An, Z. S., Clemens, S. C., Shen, J., Qiang, X. K., Jin, Z. D., Sun, Y. B., et al. (2011). Glacial-interglacial Indian Summer Monsoon dynamics. *Science*, *333*(6043), 719–723. https://doi.org/10.1126/science.1203752

An, Z. S., Kutzbach, J. E., Prell, W. L., & Porter, S. C. (2001). Evolution of Asian monsoons and phased uplift of the Himalaya-Tibetan plateau since late Miocene times. *Nature*, *311*, 62–66. https://doi.org/10.1038/35075035

Ao, H., Roberts, A. P., Dekkers, M. J., Liu, X., Rohling, E. J., Shi, Z., et al. (2016). Late Miocene–Pliocene Asian monsoon intensification linked to Antarctic ice-sheet growth. *Earth and Planetary Science Letters*, *444*, 75–87. https://doi.org/10.1016/j.epsl.2016.03.028

Araguas-Araguas, L., Froehlich, K., & Rozanski, K. (1998). Stable isotope composition of precipitation over southeast Asia. *Journal of Geophysical Research*, *103*, 28,721–28,742. https://doi.org/10.1029/98JD02582

Battisti, D. S., Ding, Q., & Roe, G. H. (2014). Coherent pan-Asian climatic and isotopic response to orbital forcing of tropical insolation. *Journal of Geophysical Research: Atmospheres*, *119*, 11,997–12,020. https://doi.org/10.1002/2014JD021960

Bohacs, K., Carroll, A., Neal, J., & Mankiewicz, P. (2000). Lake-basin type, source potential, and hydrocarbon character: An integrated sequence-stratigraphic-geochemical framework. In E. H. Gierlowski-Kordesch & K. R. Kelts (Eds.), *Lake basins through space and time*, *AAPG Studies in Geology* (pp. 3–34). Tulsa, OK: American Association of Petroleum Geologists.

Bookhagen, B., & Burbank, D. W. (2010). Toward a complete Himalayan hydrological budget: Spatiotemporal distribution of snowmelt and rainfall and their impact on river discharge. *Journal of Geophysical Research*, *115*, F03019. https://doi.org/10.1029/2009JF001426

Boos, W. R., & Kuang, Z. (2010). Dominant control the South Asian monsoon by orographic insulation versus plateau heating. *Nature*, *463*, 218–222. https://doi.org/10.1038/nature08707

Cai, Y., Fung, I. Y., Edwards, R. L., An, Z., Cheng, H., Lee, J.-E., et al. (2015). Variability of stalagmite-inferred Indian monsoon precipitation over the past 252,000 y. *Proceedings of the National Academy of Sciences*, *112*(10), 2954–2959. https://doi.org/10.1073/pnas.1424035112

Caley, T., Malaizé, B., Zaragosi, S., Rossignol, L., Bourget, J., Eynaud, F., et al. (2011). New Arabian Sea records help decipher orbital timing of Indo-Asian monsoon. *Earth and Planetary Science Letters*, *308*, 433–444. https://doi.org/10.1016/j.epsl.2011.06.019

Cane, M. A., & Molnar, P. (2001). Closing of the Indonesian seaway as a precursor to east African aridification around 3–4 million years ago. *Nature*, *411*, 157–162. https://doi.org/10.1038/35075500

Cheng, H., Edwards, R. L., Sinha, A., Spötl, C., Yi, L., Chen, S., et al. (2016). The Asian monsoon over the past 640,000 years and ice age terminations. *Nature*, *534*(7609), 640–646. https://doi.org/10.1038/nature18591

Clemens, S., Prell, W., Murray, D., Shimmield, G., & Weedon, G. (1991). Forcing mechanisms of the Indian-Ocean monsoon. *Nature*, *353*, 720–725. https://doi.org/10.1038/353720a0

Clemens, S. C., & Prell, W. L. (2003). A 350,000 year summer-monsoon multi-proxy stack from the Owen ridge, Northern Arabian sea. *Marine Geology*, *201*(1-3), 35–51. https://doi.org/10.1016/s0025-3227(03)00207-x

Clemens, S. C., Prell, W. L., Sun, Y., Liu, Z., & Chen, G. (2008). Southern Hemisphere forcing of Pliocene δ18O and the evolution of Indo-Asian monsoons. *Paleoceanography*, *23*. https://doi.org/10.1029/2008pa001638

Clift, P., Il Lee, J., Clark, M. K., & Blusztajn, J. (2002). Erosional response of South China to arc rifting and monsoonal strengthening; a record from the South China Sea. *Marine Geology*, *184*, 207–226. https://doi.org/10.1016/s0025-3227(01)00301-2

Clift, P. D., & Plumb, R. A. (2008). *The Asian Monsoon: Causes, history and effects*. Cambridge: Cambridge University Press. https://doi.org/10.1017/CBO9780511535833

Conroy, J. L., & Overpeck, J. T. (2011). Regionalization of present-day precipitation in the greater monsoon region of Asia*. *Journal of Climate*, *24*(15), 4073–4095. https://doi.org/10.1175/2011JCLI4033.1

Cui, J., Tian, L., Biggs, T. W., & Wen, R. (2017). Deuterium-excess determination of evaporation to inflow ratios of an alpine lake: Implications for water balance and modeling. *Hydrological Processes*, *31*(5), 1034–1046. https://doi.org/10.1002/hyp.11085

DeCelles, P., Quade, J., Kapp, P., Fan, M., Dettman, D., & Ding, L. (2007). High and dry in central Tibet during the Late Oligocene. *Earth and Planetary Science Letters*, *253*, 389–401. https://doi.org/10.1016/j.epsl.2006.11.001

Dettman, D., Kohn, M., Quade, J., Ryerson, F., Ojha, T., & Hamidullah, S. (2001). Seasonal stable isotope evidence for a strong Asian monsoon throughout the past 10.7 m.y. *Geology*, *29*, 31–34. https://doi.org/10.1130/0091-7613(2001)029<0031:ssiefa>2.0.co;2

Ding, L., Xu, Q., Yue, Y., Wang, H., Cai, F., & Li, S. (2014). The Andean-type Gangdese Mountains: Paleoelevation record from the Paleocene–Eocene Linzhou Basin. *Earth and Planetary Science Letters*, *392*, 250–264. https://doi.org/10.1016/j.epsl.2014.01.045

Feng, S., & Hu, Q. (2008). How the North Atlantic Multidecadal Oscillation may have influenced the Indian summer monsoon during the past two millennia. *Geophysical Research Letters*, *35*, L01707. https://doi.org/10.1029/2007GL032484

Fontes, J. C., Gasse, F., & Gibert, E. (1996). Holocene environmental changes in Lake Bangong basin (western Tibet).1. Chronology and stable isotopes of carbonates of a Holocene lacustrine core. *Palaeogeography, Palaeoclimatology, Palaeoecology*, *120*, 25–47. https://doi.org/10.1016/0031-0182(95)00032-1

Gao, J., Yao, T., & Joswiak, D. (2014). Variations of water stable isotopes (δ18O) in two lake basins, southern Tibetan Plateau. *Annals of Glaciology*, *55*(66), 97–104. https://doi.org/10.3189/2014AoG66A109

Garzione, C., Quade, J., DeCelles, P., & English, N. (2000). Predicting paleoelevation of Tibet and the Himalaya from delta O-18 vs. altitude gradients in meteoric water across the Nepal Himalaya. *Earth and Planetary Science Letters*, *183*, 215, –229. https://doi.org/10.1016/s0012-821x(00)00252-1

Garzione, C. N., Ikari, M. J., & Basu, A. R. (2005). Source of Oligocene to Pliocene sedimentary rocks in the Linxia basin in northeastern Tibet from Nd isotopes: Implications for tectonic forcing of climate. *Geological Society of America Bulletin*, *117*(9), 1156–1166. https://doi.org/10.1130/b25743.1

Gasse, F., Fontes, J. C., Van Campo, E., & Wei, K. (1996). Holocene environmental changes in Bangong Co basin (Western Tibet). Part 4: Discussion and conclusions. *Palaeogeography, Palaeoclimatology, Palaeoecology*, *120*, 79–92. https://doi.org/10.1016/0031-0182(95)00035-6

Gebregiorgis, D., Hathorne, E. C., Giosan, L., Clemens, S., Nürnberg, D., & Frank, M. (2018). Southern Hemisphere forcing of South Asian monsoon precipitation over the past ~1 million years. *Nature Communications*, *9*(1), 4702. https://doi.org/10.1038/s41467-018-07076-2

Günther, F., Witt, R., Schouten, S., Mäusbacher, R., Daut, G., Zhu, L., et al. (2015). Quaternary ecological responses and impacts of the Indian Ocean Summer Monsoon at Nam Co, Southern Tibetan Plateau. *Quaternary Science Reviews*, *112*, 66–77. https://doi.org/10.1016/j.quascirev.2015.01.023

Guo, Z. T., Ruddiman, W. F., Hao, Q. Z., Wu, H. B., Qiao, Y. S., Zhu, R. X., et al. (2002). Onset of Asian desertification by 22 Myr ago inferred from loess deposits in China. *Nature*, *416*, 159–163. https://doi.org/10.1038/416159a

Gupta, A. K., & Thomas, E. (2003). Initiation of Northern Hemisphere glaciation and strengthening of the northeast Indian monsoon: Ocean Drilling Program Site 758, eastern equatorial Indian Ocean. *Geology*, *31*(1), 47–50. https://doi.org/10.1130/0091-7613(2003)031<0047:Ionhga>2.0.Co;2

Hammer, Ø., Harper, D. A. T., & Ryan, P. D. (2001). PAST: Paleontological statistics software package for education and data analysis. *Palaeontologia Electronica*, *4*, 9.

Hays, J. D., Imbrie, J., & Shackleton, N. J. (1976). Variations in the Earth's orbit: Pacemaker of the ice ages. *Science*, *194*(4270), 1121–1132. https://doi.org/10.1126/science.194.4270.1121

Heitmann, E. O., Ji, S., Nie, J., & Breecker, D. O. (2017). Orbitally-paced variations of water availability in the SE Asian monsoon region following the Miocene climate transition. *Earth and Planetary Science Letters*, *474*, 272–282. https://doi.org/10.1016/j.epsl.2017.06.006

Herbert, T. D., Peterson, L. C., & Lawrence, K. T., Liu Z. (2010). Tropical ocean temperatures over the past 3.5 million years. *Science*, *328*(5985), 1530–1534. https://doi.org/10.1126/science.1185435

Hoke, G. D., Liu-Zeng, J., Hren, M. T., Wissink, G. K., & Garzione, C. N. (2014). Stable isotopes reveal high southeast Tibetan Plateau margin since the Paleogene. *Earth and Planetary Science Letters*, *394*, 270–278. https://doi.org/10.1016/j.epsl.2014.03.007

Huang, Y. S., Clemens, S. C., Liu, W. G., Wang, Y., & Prell, W. L. (2007). Large-scale hydrological change drove the late Miocene C-4 plant expansion in the Himalayan foreland and Arabian Peninsula. *Geology*, *35*(6), 531–534. https://doi.org/10.1130/g23666a.1

Hudson, A. M., & Quade, J. (2013). Long-term east-west asymmetry in monsoon rainfall on the Tibetan Plateau. *Geology*, *41*(3), 351–354. https://doi.org/10.1130/g33837.1

Huntington, K. W., Saylor, J. E., Quade, J., & Hudson, A. M. (2015). High late Miocene–Pliocene elevation of the Zhada Basin, southwestern Tibetan Plateau, from carbonate clumped isotope thermometry. *Geological Society of America Bulletin*, *127*(1-2), 181–199. https://doi.org/10.1130/b31000.1

Huybers, P. (2006). Early Pleistocene glacial cycles and the integrated summer insolation forcing. *Science*, *313*(5786), 508–511. https://doi.org/10.1126/science.1125249

Huybers, P. (2011). Combined obliquity and precession pacing of late Pleistocene deglaciations. *Nature*, *480*, 229. https://doi.org/10.1038/nature10626

Huybers, P., & Wunsch, C. (2005). Obliquity pacing of the late Pleistocene glacial terminations. *Nature*, *434*(7032), 491–494. https://doi.org/10.1038/nature03401

Imbrie, J., Berger, A., Boyle, E. A., Clemens, S. C., Duffy, A., Howard, W. R., et al. (1993). On the structure and origin of major glaciation cycles 2. The 100,000-year cycle. *Paleoceanography*, *8*(6), 699–735. https://doi.org/10.1029/93pa02751

Karas, C., Nurnberg, D., Gupta, A. K., Tiedemann, R., Mohan, K., & Bickert, T. (2009). Mid-Pliocene climate change amplified by a switch in Indonesian subsurface throughflow. *Nature Geoscience*, *2*, 434–438. https://doi.org/10.1038/ngeo520

Kempf, O., Blisniuk, P. M., Wang, S., Fang, X., Wrozyna, C., & Schwalb, A. (2009). Sedimentology, sedimentary petrology, and paleoecology of the monsoon-driven, fluviolacustrine Zhada Basin, SW-Tibet. *Sedimentary Geology*, *222*, 27–41. https://doi.org/10.1016/j.sedgeo.2009.07.004

Kroon, D., Steens, T., & Troelstra, S. (1991). Onset of monsoonal related upwelling in the western Arabian Sea as revealed by planktonic foraminifers. In *Proceedings of the Ocean Drilling Program: Scientific Results*, *117*, 257–263. College Station, TX: Ocean Drilling Program. https://doi.org/10.2973/odp.proc.sr.117.126.1991

Kutzbach, J., Liu, X., Liu, Z., & Chen, G. (2008). Simulation of the evolutionary response of global summer monsoons to orbital forcing over the past 280,000 years. *Climate Dynamics*, *30*, 567–579. https://doi.org/10.1007/s00382-007-0308-z

Kutzbach, J. E. (1981). Monsoon climate of the early Holocene—Climate experiment with the Earth's orbital parameters for 9000 years ago. *Science*, *214*, 59–61. https://doi.org/10.1126/science.214.4516.59

Laskar, J., Robutel, P., Joutel, F., Gastineau, M., Correia, A. C. M., & Levrard, B. (2004). A long-term numerical solution for the insolation quantities of the Earth. *Astronomy & Astrophysics*, *428*(1), 261–285. https://doi.org/10.1051/0004-6361:20041335

Lawrence, K. T., Liu, Z., & Herbert, T. D. (2006). Evolution of the eastern tropical Pacific through Plio-Pleistocene glaciation. *Science*, *312*(5770), 79–83. https://doi.org/10.1126/science.1120395

Li, H., & Ku, T. (1997). Delta C-13-delta O-18 covariance as a paleohydrological indicator for closed-basin lakes. *Palaeogeography, Palaeoclimatology, Palaeoecology*, *133*, 69–80. https://doi.org/10.1016/s0031-0182(96)00153-8

Li, H.-C., Bischoff, J. L., Ku, T.-L., Lund, S. P., & Stott, L. D. (2000). Climate variability in East-Central California during the past 1000 years reflected by high-resolution geochemical and isotopic records from Owens Lake sediments. *Quaternary Research*, *54*(2), 189–197. https://doi.org/10.1006/qres.2000.2163

Li, L., & Garzione, C. N. (2017). Spatial distribution and controlling factors of stable isotopes in meteoric waters on the Tibetan Plateau: Implications for paleoelevation reconstruction. *Earth and Planetary Science Letters*, *460*, 302–314. https://doi.org/10.1016/j.epsl.2016.11.046

Li, T., Liu, F., Abels, H. A., You, C.-F., Zhang, Z., Chen, J., et al. (2017). Continued obliquity pacing of east Asian summer precipitation after the mid-Pleistocene transition. Earth planet. *Science Letters*, *457*, 181–190. https://doi.org/10.1016/j.epsl.2016.09.045

Lisiecki, L. E., & Raymo, M. E. (2005). A Pliocene-Pleistocene stack of 57 globally distributed benthic δ18O records. *Paleoceanography*, *20*. https://doi.org/10.1029/2004PA001071

Liu, H., Sun, Z., Wang, J., & Min, J. (2004). A modeling study of the effects of anomalous snow cover over the Tibetan Plateau upon the South Asian summer monsoon. *Advances in Atmospheric Sciences*, *21*(6), 964–975. https://doi.org/10.1007/BF02915598

Liu, Z., Cleaveland, L. C., & Herbert, T. D. (2008). Early onset and origin of 100-kyr cycles in Pleistocene tropical SST records. *Earth and Planetary Science Letters*, *265*, 703–715. https://doi.org/10.1016/j.epsl.2007.11.016

Liu, Z., Wen, X., Brady, E., Otto-Bliesner, B., Yu, G., Lu, H., et al. (2014). Chinese cave records and the East Asia summer monsoon. *Quaternary Science Reviews*, *83*, 115–128. https://doi.org/10.1016/j.quascirev.2013.10.021

Lourens, L., Hilgen, F., Shackleton, N., Laskar, J., & Wilson, D. (2004). The Neogene period. In F. M. Gradstein, J. G. Ogg, & A. G. Smith (Eds.), *A geologic time scale* (pp. 409–440). Cambridge: Cambridge University Press.

Luo, Z., Su, Q., Wang, Z., Heermance, R. V., Garzione, C., Li, M., et al. (2018). Orbital forcing of Plio-Pleistocene climate variation in a Qaidam Basin lake based on paleomagnetic and evaporite mineralogic analysis. *Palaeogeography, Palaeoclimatology, Palaeoecology*, *510*, 31–39. https://doi.org/10.1016/j.palaeo.2017.09.022

Merlis, T. M., Schneider, T., Bordoni, S., & Eisenman, I. (2013). Hadley circulation response to orbital precession. Part II: Subtropical continent. *Journal of Climate*, *26*, 754–771. https://doi.org/10.1175/jcli-d-12-00149.1

Milankovitch, M. (1941). *Kanon der Erdbestrahlung und Seine Anwendung auf das Eiszeitenproblem (Canon of insolation and the ice-age problem)*, *Royal Serbian Academy of Sciences Special Publications*, *132*, Jerusalem: Israel Program for Scientific Translations.

Mohtadi, M., Prange, M., Oppo, D. W., De Pol-Holz, R., Merkel, U., Zhang, X., et al. (2014). North Atlantic forcing of tropical Indian Ocean climate. *Nature*, *509*(7498), 76–80. https://doi.org/10.1038/nature13196

Molnar, P. (2005). Mio-pliocene growth of the Tibetan Plateau and evolution of East Asian climate. *Palaeontologia Electronica*, *8*.

Morrill, C., Overpeck, J. T., Cole, J. E., Liu, K. B., Shen, C. M., & Tang, L. Y. (2006). Holocene variations in the Asian monsoon inferred from the geochemistry of lake sediments in central Tibet. *Quaternary Research*, *65*(02), 232–243. https://doi.org/10.1016/j.yqres.2005.02.014

Mudelsee, M., & Raymo, M. E. (2005). Slow dynamics of the Northern Hemisphere glaciation. *Paleoceanography*, *20*. https://doi.org/10.1029/2005pa001153

Muller, R. A., & MacDonald, G. J. (2002). *Ice ages and astronomical causes: Data, spectral analysis and mechanisms*. Berlin and Heidelberg: Springer-Verlag.

Nie, J. (2018). The Plio-Pleistocene 405-kyr climate cycles. *Palaeogeography, Palaeoclimatology, Palaeoecology*, *510*, 26–30. https://doi.org/10.1016/j.palaeo.2017.07.022

Nie, J., Garzione, C., Su, Q., Liu, Q., Zhang, R., Heslop, D., et al. (2017). Dominant 100,000-year precipitation cyclicity in a late Miocene lake from Northeast Tibet. *Science Advances*, *3*, e1600762. https://doi.org/10.1126/sciadv.1600762

Nie, J., Stevens, T., Song, Y., King, J. W., Zhang, R., Ji, S., et al. (2014). Pacific freshening drives Pliocene cooling and Asian monsoon intensification. *Scientific Reports*, *4*(1), 5474. https://doi.org/10.1038/srep05474

Prell, W., & Kutzbach, J. (1992). Sensitivity of the Indian monsoon to forcing parameters and implications for its evolution. *Nature*, *360*, 647–652. https://doi.org/10.1038/360647a0

Quade, J., Breecker, D. O., Daeron, M., & Eiler, J. (2011). The paleoaltimetry of Tibet: An isotopic perspective. *American Journal of Science*, *311*(2), 77–115. https://doi.org/10.2475/02.2011.01

Quade, J., Cater, J., Ojha, T., Adam, J., & Harrison, T. (1995). Late Miocene environmental change and in Nepal and the northern Indian subcontinent; stable isotopic evidence from paleosols. *Geological Society of America Bulletin*, *107*, 1381–1397. https://doi.org/10.1130/0016-7606(1995)107<1381:lmecin>2.3.co;2

Rajagopalan, B., & Molnar, P. (2013). Signatures of Tibetan Plateau heating on Indian summer monsoon rainfall variability. *Journal of Geophysical Research: Atmospheres*, *118*, 1170–1178. https://doi.org/10.1002/jgrd.50124

Rea, D. K., Snoeckx, H., & Joseph, L. H. (1998). Late Cenozoic eolian deposition in the North Pacific: Asian drying, Tibetan uplift, and cooling of the northern hemisphere. *Paleoceanography*, *13*(3), 215–224. https://doi.org/10.1029/98pa00123

Rowley, D. B., Pierrehumbert, R. T., & Currie, B. S. (2001). A new approach to stable isotope-based paleoaltimetry: Implications for paleoaltimetry and paleohypsometry of the High Himalaya since the Late Miocene. *Earth and Planetary Science Letters*, *188*, 253–268. https://doi.org/10.1016/s0012-821x(01)00324-7

Rowley, D. B. (2007). Stable isotope-based paleoaltimetry: Theory and validation. In *Paleoaltimetry: Geochemical and Thermodynamic Approaches*, *Reviews in Mineralogy and Geochemistry*, *66*, 23–52. Chantilly, Virginia: Mineralogical Society of America.

Ruddiman, W. F. (2001). *Earth's Climate: Past and Future* (3rd ed.). New York: Macmillan.

Saylor, J. E., Casturi, L., Shanahan, T. M., Nie, J., & Saadeh, C. M. (2016). Tectonic and climate controls on Neogene environmental change in the Zhada Basin, southwestern Tibetan Plateau. *Geology*, *44*(11), 919–922. https://doi.org/10.1130/g38173.1

Saylor, J. E., DeCelles, P. G., Gehrels, G., Murphy, M., Zhang, R., & Kapp, P. (2010a). Basin formation in the High Himalaya by arc-parallel extension and tectonic damming: Zhada basin, southwestern Tibet. *Tectonics*, *29*(1), TC1004. https://doi.org/10.1029/2008TC002390

Saylor, J. E., DeCelles, P. G., & Quade, J. (2010b). Climate-driven environmental change in the Zhada basin, southwestern Tibetan Plateau. *Geosphere*, *6*(2), 74–92. https://doi.org/10.1130/ges00507.1

Saylor, J. E., Nie, J., & Shanahan, T. M. (2013). *Sequence stratigraphy and the stable isotope record of the Zhada Basin, SW Tibet: Implications for paleoelevation research, Geological Society of America Annual Meeting, Denver, CO*. Boulder, CO: Geological Society of America.

Saylor, J. E., Quade, J., Dettman, D. L., DeCelles, P. G., Kapp, P. A., & Ding, L. (2009). The late Miocene through present paleoelevation history of southwestern Tibet. *American Journal of Science*, *309*(1), 1–42. https://doi.org/10.2475/01.2009.01

Schulz, M., & Mudelsee, M. (2002). REDFIT: Estimating red-noise spectra directly from unevenly spaced paleoclimatic time series. *Computational Geosciences*, *28*, 421–426. https://doi.org/10.1016/S0098-3004(01)00044-9

Senan, R., Orsolini, Y. J., Weisheimer, A., Vitart, F., Balsamo, G., Stockdale, T. N., et al. (2016). Impact of springtime Himalayan–Tibetan Plateau snowpack on the onset of the Indian summer monsoon in coupled seasonal forecasts. *Climate Dynamics*, *47*(9-10), 2709–2725. https://doi.org/10.1007/s00382-016-2993-y

Shi, X., Zhang, F., Tian, L., Joswiak, D. R., Zeng, C., & Qu, D. (2014). Tracing contributions to hydro-isotopic differences between two adjacent lakes in the southern Tibetan Plateau. *Hydrological Processes*, *28*(22), 5503–5512. https://doi.org/10.1002/hyp.10051

Su, Q., Nie, J., Saylor, J. E., Horton, B. K., Bush, M. A., & Chen, W. (2016). An anisotropy of magnetic susceptibility study of the Cenozoic Dahonggou section in northern Qaidam Basin and its tectonic implications. *Quaternary Sciences (in Chinese)*, *36*, 859–869. https://doi.org/10.11928/j.issn.1001-7410.2016.04.07

Su, T., Farnsworth, A., Spicer, R. A., Huang, J., Wu, F.-X., Liu, J., et al. (2019). No high Tibetan Plateau until the Neogene. *Science Advances*, *5*, eaav2189. https://doi.org/10.1126/sciadv.aav2189

Sun, Y., & An, Z. (2005). Late Pliocene-Pleistocene changes in mass accumulation rates of eolian deposits on the central Chinese Loess Plateau. *Journal of Geophysical Research*, *110*, D23101. https://doi.org/10.1029/2005JD006064

Talbot, M. R. (1990). A review of the paleohydrological interpretation of carbon and oxygen isotopic-ratios in primary lacustrine carbonates. *Chemical Geology*, *80*, 261–279. https://doi.org/10.1016/0168-9622(90)90009-2

Tang, H., Micheels, A., Eronen, J. T., Ahrens, B., & Fortelius, M. (2013). Asynchronous responses of East Asian and Indian summer monsoons to mountain uplift shown by regional climate modelling experiments. *Climate Dynamics*, *40*(5-6), 1531–1549. https://doi.org/10.1007/s00382-012-1603-x

Terray, P., Delecluse, P., Labattu, S., & Terray, L. (2003). Sea surface temperature associations with the late Indian summer monsoon. *Climate Dynamics*, *21*(7-8), 593–618. https://doi.org/10.1007/s00382-003-0354-0

Tian, L., Yao, T., Numaguti, A., & Sun, W. (2001). Stable isotope variations in monsoon precipitation on the Tibetan Plateau. *Journal of the Meteorological Society of Japan*, *79*, 959–966. https://doi.org/10.2151/jmsj.79.959

Tiedemann, R., Sarnthein, M., & Shackleton, N. J. (1994). Astronomic timescale for the Pliocene Atlantic δ18O and dust flux records of Ocean Drilling Program Site 659. *Paleoceanography*, *9*, 619–638. https://doi.org/10.1029/94PA00208

Torrence, C., & Compo, G. P. (1998). A practical guide to wavelet analysis. *Bulletin of the American Meteorological Society*, *79*(1), 61–78. https://doi.org/10.1175/1520-0477(1998)079<0061:apgtwa>2.0.co;2

Vernekar, A., Zhou, J., & Shukla, J. (1995). The effect of Eurasian snow cover on the Indian monsoon. *Journal of Climate*, *8*, 248–266. https://doi.org/10.1175/1520-0442(1995)008<0248:teoesc>2.0.co;2

Vuille, M., Werner, M., Bradley, R. S., & Keimig, F. (2005). Stable isotopes in precipitation in the Asian monsoon region. *Journal of Geophysical Research*, *110*, D23108. https://doi.org/10.1029/2005jd006022

Wang, B., Clemens, S. C., & Liu, P. (2003). Contrasting the Indian and East Asian monsoons: Implications on geologic timescales. *Marine Geology*, *201*, 5–21. https://doi.org/10.1016/s0025-3227(03)00196-8

Wang, B., Wu, R., & Lau, K. (2001). Interannual variability of the Asian summer monsoon: Contrasts between the Indian and the western North Pacific–East Asian monsoons. *Journal of Climate*, *14*, 4073–4090. https://doi.org/10.1175/1520-0442(2001)014<4073:ivotas>2.0.co;2

Wang, P. X., Clemens, S., Beaufort, L., Braconnot, P., Ganssen, G., Jian, Z. M., et al. (2005). Evolution and variability of the Asian monsoon system: State of the art and outstanding issues. *Quaternary Science Reviews*, *24*(5-6), 595–629. https://doi.org/10.1016/j.quascirev.2004.10.002

Wang, P. X., Wang, B., Cheng, H., Fasullo, J., Guo, Z., Kiefer, T., & Liu, Z. (2017). The global monsoon across time scales: Mechanisms and outstanding issues. *Earth-Science Reviews*, *174*, 84–121. https://doi.org/10.1016/j.earscirev.2017.07.006

Wang, R. L., Scarpitta, S. C., Zhang, S. C., & Zheng, M. P. (2002). Later Pleistocene/Holocene climate conditions of Qinghai-Xizhang Plateau (Tibet) based on carbon and oxygen stable isotopes of Zabuye Lake sediments. *Earth and Planetary Science Letters*, *203*(1), 461–477. https://doi.org/10.1016/s0012-821x(02)00829-4

Winkler, M. G., & Wang, P. K. (1993). The late-Quaternary vegetation and climate of China. In H. E. Wright, J. E. Kutzbach, T. Webb III, W. F. Ruddiman, F. A. Street-Perrott, & P. J. Bartlein (Eds.), *Global Climates since the Last Glacial Maximum* (pp. 221–264). Minneapolis, MN: University of Minnesota Press.

Wu, F., Herrmann, M., & Fang, X. (2014). Early Pliocene paleo-altimetry of the Zanda Basin indicated by a sporopollen record. *Palaeogeography, Palaeoclimatology, Palaeoecology*, *412*, 261–268. https://doi.org/10.1016/j.palaeo.2014.08.006

Xinzhou, L., Xiaodong, L., & Hongli, Z. (2017). Transient simulation of the Tibetan Plateau modulated distinct orbital-scale precipitation variation in East and South Asia. *Palaeogeography, Palaeoclimatology, Palaeoecology*, *485*, 899–905. https://doi.org/10.1016/j.palaeo.2017.08.005

Yao, T., Masson-Delmotte, V., Gao, J., Yu, W., Yang, X., Risi, C., et al. (2013). A review of climatic controls on δ18O in precipitation over the Tibetan Plateau: Observations and simulations. *Reviews of Geophysics*, *51*, 525–548. https://doi.org/10.1002/rog.20023

Yu, W., Yao, T., Tian, L., Ma, Y., Kurita, N., Ichiyanagi, K., et al. (2007). Stable isotope variations in precipitation and moisture trajectories on the Western Tibetan Plateau, China. *Arctic, Antarctic, and Alpine Research*, *39*(4), 688–693. https://doi.org/10.1657/1523-0430(07-511)[YU]2.0.CO;2

Yuan, D., Cheng, H., Edwards, R. L., Dykoski, C. A., Kelly, M. J., Zhang, M., et al. (2004). Timing, duration, and transitions of the last interglacial Asian monsoon. *Science*, *304*, 575–578. https://doi.org/10.1126/science.1091220

Yuan, F., Sheng, Y., Yao, T., Fan, C., Li, J., Zhao, H., & Lei, Y. (2011). Evaporative enrichment of oxygen-18 and deuterium in lake waters on the Tibetan Plateau. *Journal of Paleolimnology*, *46*(2), 291–307. https://doi.org/10.1007/s10933-011-9540-y

Zhang, R., Jiang, D., Zhang, Z., & Yu, E. (2015). The impact of regional uplift of the Tibetan Plateau on the Asian monsoon climate. *Palaeogeography, Palaeoclimatology, Palaeoecology*, *417*, 137–150. https://doi.org/10.1016/j.palaeo.2014.10.030

Zhang, T., Wang, T., Krinner, G., Wang, X., Gasser, T., Peng, S., et al. (2019). The weakening relationship between Eurasian spring snow cover and Indian summer monsoon rainfall. *Science Advances*, *5*, eaau8932. https://doi.org/10.1126/sciadv.aau8932

Zhu, D., Meng, X., Shoa, Z., Yang, C., Han, J., Yu, J., et al. (2007). Evolution of the paleovegatation, paleoenvironment and paleoclimate during Pliocene - early Pleistocene in Zhada Basin, Ali, Tibet. *Acta Geologica Sinica*, *81*, 295–306.

Zhu, L. P., Zhen, X. L., Wang, J. B., Lu, H. Y., Xie, M. P., Kitagawa, H., & Possnert, G. (2009). A similar to 30,000-year record of environmental changes inferred from Lake Chen Co, Southern Tibet. *Journal of Paleolimnology*, *42*(3), 343–358. https://doi.org/10.1007/s10933-008-9280-9